J. Fluid Mech. (2014), *vol.* 759, *pp.* 546–578.
doi:10.1017/jfm.2014.576

On the modulating effect of three-dimensional instabilities in open cavity flows

J. Basley[1,2,3,†], L. R. Pastur[1,2], F. Lusseyran[1], J. Soria[3,4] and N. Delprat[1,5]

[1]CNRS, Laboratoire d'Informatique pour la Mécanique et les Sciences de l'Ingénieur (LIMSI), F-91403 Orsay, France

[2]Univ. Paris-Sud, F-91405 Orsay, France

[3]Laboratory for Turbulence Research in Aerospace and Combustion (LTRAC), Department of Mechanical and Aerospace Engineering, Monash University, Victoria, 3800, Australia

[4]Department of Aeronautical Engineering, King Abdulaziz University, Jeddah, Kingdom of Saudi Arabia

[5]Sorbonne Universités, UPMC Univ. Paris 6, UFR d'Ingénierie, F-75005 Paris, France

(Received 30 March 2014; revised 18 August 2014; accepted 28 September 2014)

Open cavity flows are known to select and enhance locked-on modes or tones. High-energy self-sustained oscillations arise within the shear layer, impinging onto the trailing edge of the cavity. These self-sustained oscillations are subject to amplitude modulations (AMs) at multiple low frequencies. However, only a few studies have addressed the identification of the lowest modulating frequencies. The present work brings to light salient AMs of the shear layer waves and identifies their source as three-dimensional dynamics existing inside the cavity. Indeed, the recirculating inner flow gives rise to centrifugal instabilities, which entail broad-band frequencies down two orders of magnitude lower than those of the self-sustained oscillations. Using time-resolved PIV (TRPIV) in two planes, the nonlinearly saturated dynamics is analysed in both space and time by means of proper orthogonal decomposition, global Fourier decomposition and Hilbert–Huang transforms. The inner flow can be decomposed as three-dimensional waves carried by the main recirculation. Bicoherence distributions are computed to highlight the nonlinear interactions between these spanwise-travelling waves inside the cavity and the locked-on modes. The modulated envelope of the shear layer oscillations is extracted and investigated with regards to the inner-flow dynamics. Strong cross-correlations, in time rather than in space, reveal a global coupling mechanism, possibly related to the beating of the spanwise-travelling waves.

Key words: instability, shear layers, vortex flows

1. Introduction

A separated flow over an open cavity (figure 1) is primarily characterised by the enhancement of self-sustained oscillations. As the incoming flow passes successively backward- and forward-facing steps – making a rectangular cavity – Kelvin–Helmholtz travelling waves arise in the shear layer and lock on the cavity length L due to an acoustic feedback loop between impingement and separation (Powell 1953, 1995).

† Email address for correspondence: jeremy.basley@ladhyx.polytechnique.fr

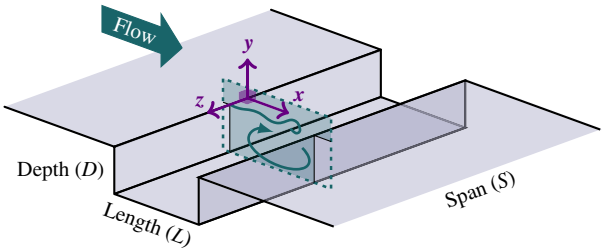

FIGURE 1. (Colour online) Sketch of the geometry under study. Flow features are illustrated in the (x, y)-plane (normal to the bottom of the cavity).

These locked-on waves translate into self-sustained oscillations of the shear layer. Spectrally, they correspond to a series of well-defined peaks, whose non-harmonic distribution has been empirically modelled in the compressible regime by Rossiter (1964). When the flow is incompressible, the acoustic feedback can be considered as instantaneous. The locked-on frequencies f_n thus approximately satisfy the simple expression

$$f_n L/U_0 \approx n/2, \tag{1.1}$$

where U_0 is the external velocity and $n \in \mathbb{N}^*$ is the number of cycles between separation and reattachment. Consider a laminar incoming flow, for which θ_0 is the momentum thickness of the boundary layer at separation. The dimensionless cavity length L/θ_0 is the primary control parameter of the self-sustaining phenomenon (Powell 1961; Sarohia 1977; Rockwell & Naudascher 1978; Yamouni, Sipp & Jacquin 2013).

1.1. *Motivation*

Self-sustained oscillations and vortex–edge interactions are responsible for noise generation and drag. They can also lead to structural damage. As such, impinging shear layer waves and associated amplitude modulations (AMs) have been of primary interest in the literature, notably in the extensive work of Rockwell and coworkers (Rockwell 1977; Knisely & Rockwell 1982; Ziada & Rockwell 1982). On the other hand, very low modulating frequencies – more than 10 times lower than locked-on frequencies – are generally disregarded. AMs at such very low frequencies have still been unambiguously identified in several studies (Neary & Stephanoff 1987; Kegerise *et al.* 2004; Delprat 2006; Malone *et al.* 2009; Delprat 2010; Vikramaditya & Kurian 2012). An illustration of such a phenomenon is given in figure 2. In terms of signal processing, the shear layer locked-on mode constitutes a carrier wave with an envelope evolving over much larger time scales. In dimensionless time based on external velocity and cavity depth, $t\,U_0/D$, the period of the carrier wave is 2 while the period of the envelope is around 40; that is, 20 times larger. The snapshots of the vorticity fluctuations in figure 2(*b,c*) show the spatial dynamics of the flow corresponding respectively to high- and low-amplitude oscillations in the time series. Intense vortices impinging onto the cavity edge are observed when the envelope is maximal, while shear layer waves are drastically damped when the envelope is close to zero.

This work demonstrates that similar AMs by very low frequencies occur consistently in different experiments and for a wide range of control parameters. An understanding

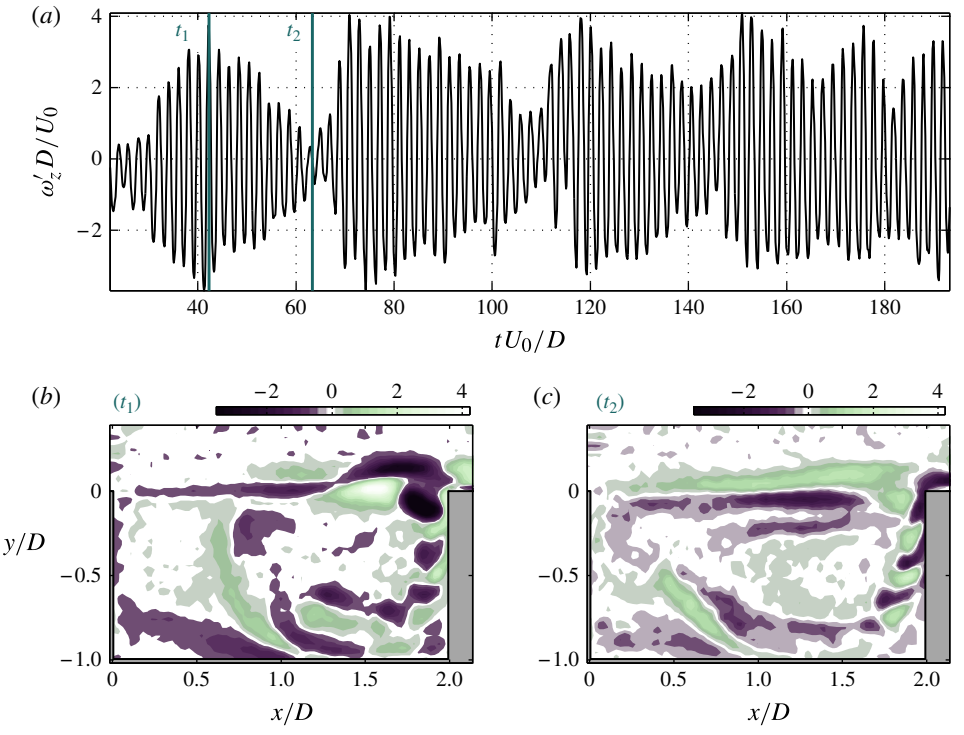

FIGURE 2. (Colour online) Vorticity fluctuations $\omega_z' D/U_0$ of time-resolved particle image velocimetry (TRPIV) data in an (x, y)-plane, for $L/D = 2.0$ and $L/\theta_0 = 82$ ($U_0 = 1.38$ m s^{-1}). (*a*) Time series extracted at $(x, y) = (1.5D, 0)$. (*b,c*) Two snapshots characteristic of high-amplitude and low-amplitude oscillations, respectively.

of such a consistent pattern related to severe flow variations could turn out to be crucial for the quantification and control of the shear layer locked-on waves. To this end, the present work identifies the source of the lowest frequencies in open cavity flows, as well as their effects on the self-sustained oscillations of the impinging shear layer.

1.2. *Three-dimensional dynamics in cavity flows*

In studies dealing with self-sustained oscillations of the shear layer, open cavity flows are often considered as two-dimensional to a first approximation. The spanwise extension of the flow may still have non-negligible influence on the secondary features. This was notably developed by Larchevêque, Sagaut & Labbé (2007), who addressed the occurrence of symmetry breakings, associated with spanwise fluctuations of the inner flow. In Neary & Stephanoff (1987) and more recently in Delprat (2010), the three-dimensional organisation of the flow was also pointed out to interpret AMs of shear layer waves by very low frequencies.

The first three-dimensional effects are concerned with the influence of the spanwise boundary conditions. In strict terms, spanwise-invariant basic states require that endwalls be non-existent; that is, either periodical spanwise boundary conditions or infinite span ($S \to \infty$). However, in practice, the presence of endwalls is prevalent, which makes the basic state three-dimensional. The influence of the endwalls depends

on the cavity span/depth ratio S/D. We state that cavity geometries can be split into two classes.

(i) Cavities where $S \sim D$ constitute fully three-dimensional geometries with no salient direction in the flow. Such systems are not treated here but have notably been investigated in Larchevêque *et al.* (2004) and Woo, Kim & Lee (2007).

(ii) Cavities with larger spanwise extensions – basically where $S/D > 4$ – involve almost two-dimensional flows; that is, mainly streamwise–crosswise dynamics. Nevertheless, no-slip spanwise boundary conditions do have secondary effects. According to observations of Koseff & Street (1984*b*), Guermond *et al.* (2002) and Migeon, Pineau & Texier (2003) in lid-driven cavities, a steady centripetal flow forms at the endwalls. Similarly to what is observed in Bödewadt layers (Bödewadt 1940; Fernandez-Feria 2000), the outer flow of the main recirculation is drawn towards the endwalls while a counter-flow is reinjected along the centreline. In Albensoeder, Kuhlmann & Rath (2001), endwalls result in buffer regions encompassing about a quarter of the span. In open cavities, the suction induced by endwall layers is also reported by Faure *et al.* (2007, 2009), but the buffer regions are much smaller.

From now on, we only consider cavities with large spanwise extension. These primarily two-dimensional flows are subject to basically two types of three-dimensional instabilities: secondary instabilities in the impinging shear layer and centrifugal instabilities within the recirculating flow.

The first type of three-dimensional (3D) instability is intrinsic to the shear layer developing over the cavity. Shear flows are known to bifurcate from 2D vortex shedding towards three-dimensionally organised dynamics through secondary instabilities (Taylor 1923). In particular, the three-dimensional nature of impinging flows was first reported by Görtler (1955). Following the work of Benney & Lin (1960), Miksad (1972) demonstrated that 3D dynamics can be produced by nonlinear wave interactions in free shear layers. Rockwell and coworkers applied the same approach to shear layers impinging onto an edge, notably in Rockwell & Naudascher (1979). Very low frequencies were not specifically mentioned, but the perturbation of the locked-on waves by three-dimensional dynamics was incontestable. In Rockwell & Knisely (1980), shear layer travelling waves underwent important spanwise distortions in the form of streamwise vortices. Streamwise vorticity was described as 'three-dimensionalities enhanced and mitigated in the impingement region'. The 'upstream convection of non-uniformities' was only mentioned as a secondary effect. Although experimental techniques could not give access to the precise characteristics of 3D dynamics at the time, spanwise wavelengths were approximated to the order or half the order of the streamwise wavelength.

Since then, the secondary instability of free shear layers has continued to be the subject of numerous experimental studies, among which are the works by Jimenez (1983) and Lasheras & Choi (1988). The physical mechanism at play was described as the strain induced between two shed vortices giving rise to streamwise vortex tubes. The spanwise length scale associated with these streamwise vortex tubes largely depends on the initial conditions. The sensibility to the initial conditions at separation was notably demonstrated by Lasheras & Choi (1988). They made use of corrugated plates to initialise the free shear layers with sinusoidal perturbation of various spanwise wavelengths. These conclusions were supported by the numerical investigation of Metcalfe *et al.* (1987), who showed that plane shear layers are unstable with regards to 3D perturbations for a wide range of spanwise wavenumbers.

Another three-dimensional instability is at play in cavity flows regardless of the shear layer vortex shedding. The recirculating flow inside the cavity can undergo centrifugal instabilities. For the past three decades, the bifurcation of initially two-dimensional recirculating flows towards three-dimensional states has indeed received noticeable attention.

Over the years, linear stability analyses have consistently shown that recirculating flows become globally unstable with regards to spanwise-periodic disturbances for relatively low Reynolds numbers. The recirculating flow bifurcates from a steady (two-dimensional) basic state towards a three-dimensionally structured flow. The onset of such 3D disturbances is attributed to centrifugal instabilities (Sipp & Jacquin 2000). This was notably observed in the case of a recirculation induced by a backward-facing step; see, for instance, Barkley, Gomes & Henderson (2002) and Beaudoin *et al.* (2004). Cavity flows belong to the same class of recirculating flows. Lid-driven cavities are subject to the rise of spanwise waves along the steady recirculation (Ramanan & Homsy 1994; Albensoeder *et al.* 2001; Theofilis 2003; Gonzalez *et al.* 2011) as well as open cavities (Brès & Colonius 2008; Meseguer-Garrido *et al.* 2011; de Vicente *et al.* 2014; Meseguer-Garrido *et al.* 2014). Global stability analyses have shown that marginal stability curves actually depend on multiple control parameters, all based on the cavity depth D, from the Reynolds number Re_D to the dimensionless boundary layer thickness θ_0/D and the cavity shape ratio L/D. The underlying control parameter is in fact the Rayleigh discriminant along the recirculating flow inside the cavity. Indeed, Rayleigh discriminant distributions demonstrate that basic states are centrifugally unstable within the shear regions between the curved streamlines of the recirculation and the cavity walls. This is evidenced notably in Brès & Colonius (2008) for open cavity flows. Based on experimental mean flows, figure 3 reproduces similar results but shows at the impingement another strongly centrifugally unstable region, probably due to higher control parameters. One should note also the spiral-like streamlines that entail an out-of-plane flow within the main recirculation. Unstable eigenmodes resulting from centrifugal instabilities organise as spanwise waves, either steady or travelling. The growing disturbances wind around the main recirculation and scale on the cavity depth D. The corresponding wavenumbers β are typically such that

$$4 \lesssim \beta = \frac{2\pi D}{\lambda_z} \lesssim 15, \tag{1.2}$$

where λ_z is the spanwise wavelength (Albensoeder *et al.* 2001; Brès & Colonius 2008; Meseguer-Garrido *et al.* 2011; Basley 2012; de Vicente *et al.* 2014; Meseguer-Garrido *et al.* 2014). It is important to note that all unstable travelling eigenmodes reported in the literature are associated with particularly low frequencies – see Chiang, Sheu & Hwang (1998), Theofilis (2003), Theofilis, Duck & Owen (2004), Brès & Colonius (2008) and references therein. Very recently, the extensive parametric study presented by Meseguer-Garrido *et al.* (2014) has identified the unstable and least stable branches of oscillating eigenmodes for a wide range of parameters. In brief, the frequencies f_{ci} entailed by centrifugal instabilities are comprised in the range of Strouhal numbers based on cavity depth

$$St_{ci} = f_{ci} D/U_0 \lesssim 0.05. \tag{1.3}$$

In the saturated regime, the spanwise waves embodied by the eigenmodes develop into alleys of counter-rotating vortex pairs coiled around the recirculating flow. Numerous studies on both lid-driven and shear-driven cavities have reported the appearance of such salient spiral eddies – often referred to as Taylor–Görtler-type

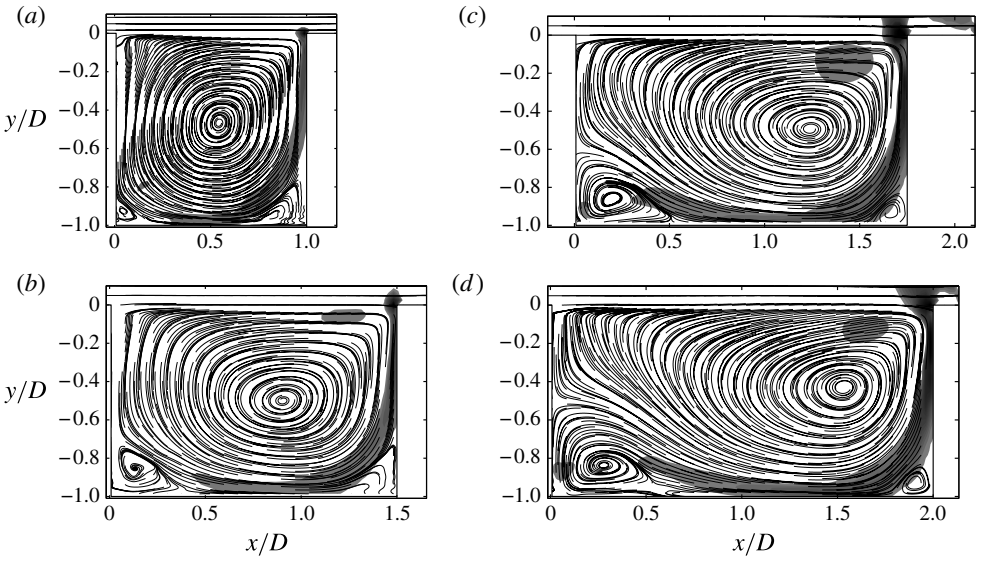

FIGURE 3. Streamlines and distribution of the Rayleigh discriminant η calculated using the mean flow computed from PIV data in a plane normal to the bottom of the cavity (see § 2.1 for details). Shaded areas correspond to $\eta > 0$. (*a*) $L/D = 1.0$, $L/\theta_0 = 54$; (*b*) $L/D = 1.5$, $L/\theta_0 = 70$; (*c*) $L/D = 1.75$, $L/\theta_0 = 96$; (*d*) $L/D = 2.0$, $L/\theta_0 = 96$. See the similar study in Brès & Colonius (2008) for details and comparison.

vortices – spanwise-distributed within the inner flow. Lid-driven cavities have often been preferred as they offer controlled and simple boundary conditions, avoiding any external influence. Various geometries have been investigated, from one-sided lid-driven rectangular cavities (Koseff & Street 1984*a*,*b*,*c*; Aidun, Triantafillopoulos & Benson 1991; Chiang *et al.* 1998; Albensoeder *et al.* 2001; Migeon *et al.* 2003; Theofilis *et al.* 2004; Albensoeder & Kuhlmann 2006) to two-sided driven cavities (Kuhlmann, Wanschura & Rath 1997; de Vicente 2010), from triangular cavities (Gonzalez *et al.* 2011) to periodically driven cavities (Blackburn & Lopez 2003; Vogel, Hirsa & Lopez 2003). In every case, spanwise-periodic dynamics spontaneously arise and organise as Taylor–Görtler-type vortices whose wavelengths $\lambda_z \sim D$ fairly match those of the eigenmodes. Open cavity flows involve more complexity caused by shear layer vortex shedding. However, the inner flow remains mainly steady and still resembles that of a lid-driven cavity for sufficiently low L/θ_0. Recent studies dealing with open cavities have indeed reported spanwise wave alleys of Taylor–Görtler-type vortices, both experimentally (Faure *et al.* 2007; Douay *et al.* 2011; Basley 2012; Basley *et al.* 2014; de Vicente *et al.* 2014) and in simulations (Brès & Colonius 2008; Faure *et al.* 2009).

When the dimensionless cavity length L/θ_0 increases, the shear layer that develops above an open cavity becomes strongly unstable. Self-sustained oscillations induce unsteadiness, mixing with the inner flow. An unsteady base flow entails different stability properties as the fast-scale disturbances from the shear layer might disrupt the growth of slower three-dimensional dynamics. On the other hand, the mixing implied by shear layer flapping motion amplifies the recirculation; hence, it enhances the centrifugal effects inside the cavity. In fact, observations suggest that Taylor–Görtler vortices actually endure in spite of the shear layer disturbances. For instance, the

direct numerical simulations by Chang, Constantinescu & Park (2006), Podvin *et al.* (2006) and Brès & Colonius (2008) reveal inner-flow spanwise waves coexisting with Kelvin–Helmholtz vortex shedding. Recently, this coexistence was also observed in an experimental study by the authors (Basley *et al.* 2013) and in Guéniat, Pastur & Lusseyran (2014).

If both phenomena can coexist, nonlinear interactions between inner-flow centrifugal instabilities and shear layer waves are likely to occur. To the best of the authors' knowledge, the link between the spanwise dynamics inside the cavity and AMs of the shear layer oscillations was first observed in Neary & Stephanoff (1987). There, oscillations at the locked-on frequency were modulated by a frequency about ten times lower. The modulating frequency was interpreted as the result of spanwise time variations of the main recirculation. Later, Pereira & Sousa (1995) also attributed low-frequency modulations to the recirculating flow inside the cavity. In addition, the works of Delprat (2006, 2010) used a signal processing approach to highlight the impact of AMs on compressible cavity flows. In Delprat (2006), the Rossiter formula was reinterpreted through modulations by a low frequency. Then, Delprat (2010) proposed a model based on the combination of two modulation mechanisms to connect Rossiter modes with low frequencies. Interestingly, the lowest modulating frequencies identified in Delprat (2010) were systematically consistent with time scales typically associated with inner-flow centrifugal instabilities (expression (1.3)). These studies and observations all suggest that some AM process of the shear layer oscillations might be directly induced by Taylor–Görtler vortices inside the cavity.

Should such a connection between inner-flow centrifugal instabilities and shear layer waves exist, the nonlinear coupling may be either (i) local, that is, dependent on the position in the flow, or (ii) global. Scenario (i) relies on local nonlinearities at play between the shear layer vortices – the carrier wave – and the slow-moving 3D vortices filling the inner flow – the low-frequency source. As this source implies both temporal and spanwise fluctuations, the AM is expected to vary along the span. In contrast, hypothesis (ii) involves a global modulation, for which the envelope of the shear layer remains basically spanwise-invariant. In this respect the coupling takes place regardless of the spatial extension of the flow and the AM is temporal only.

1.3. *Outline of the study*

The previous section has reviewed the three-dimensional instabilities at play in open cavity flows. The 3D effects are generally investigated apart from the self-sustaining mechanism. In contrast, this work focuses on the influence of 3D instabilities on the locked-on waves of the shear layer.

The study is based on two experimental campaigns, which are described in § 2. The 3D organisation of the flow is investigated using time-resolved particle image velocimetry (TRPIV) measurements in two planes.

The discussion of the results encompasses §§ 3–5. We demonstrate that centrifugal instabilities arising in the inner flow are responsible for drastic modulations of the self-sustained oscillations.

In § 3, the lowest frequencies of the flow are identified throughout the parameter space. Nonlinear interactions between these very low frequencies and the shear layer locked-on modes are ascertained and correspond to AMs of the self-sustained oscillations of the shear layer.

In § 4, the spatial dynamics associated with the very low modulating frequencies is identified as slow-moving large-scale structures that coil up inside the cavity. The

Campaign	L/D	U_0 (m s^{-1})	Re_D [a]	Re_{θ_0} [b]	L/θ_0	θ_0/D	$f_s D/U_0$ [c]
(x, y)-plane (LIMSI, wind tunnel)	1	2.42	7700	143	54	0.019	5.2
	1.5	1.77	5870	126	70	0.021	7.1
	1.5	2.10	6800	135	76	0.020	6.0
	1.5	2.31	7470	141	79	0.019	5.4
	1.5	2.81	9400	161	88	0.017	4.4
	1.5	2.89	9730	164	89	0.017	4.3
	1.75	2.48	8060	146	96	0.018	5.0
	2	1.38	4550	111	82	0.024	9.1
	2	1.71	5750	126	91	0.022	7.3
	2	1.89	6350	132	96	0.021	6.6
	2	2.18	7250	141	103	0.019	5.7
(z, x)-plane (LTRAC, water tunnel)	2	0.0295	1500	65	46	0.043	0.57
	2	0.0475	2400	81	59	0.034	0.39

[a] Reynolds number based on cavity depth, [b] based on momentum thickness at separation, [c] dimensionless sampling frequency.

TABLE 1. Characteristics and control parameters of the TRPIV campaigns.

spanwise extension of the flow is investigated: the inner flow experiences highly coherent spanwise undulations. These three-dimensional waves are characteristic of the centrifugal instabilities along the recirculating flow.

In § 5, the study concentrates on the mechanism of interaction between centrifugal instabilities and shear layer waves. The results show unvaryingly a strong time correlation between the AM of the shear layer and the slow dynamics of the inner flow. The modulation is almost strictly temporal, which indicates a global coupling. The spanwise time correlations suggest that the coupling is related to a beating induced by interference of the spanwise travelling waves.

Our conclusions are presented in § 6.

2. Experiments

This work is based on experimental results obtained from two TRPIV campaigns, whose parameters are listed in table 1. On the one hand, wind-tunnel experiments (LIMSI) focus on the primary dynamics of the flow, that is the shear layer waves and the recirculating flow inside the cavity. On the other hand, the water-tunnel campaign (LTRAC) is concerned with the spanwise extension of the flow.

2.1. *High-frame-rate PIV in a normal plane*

For the experimental campaign at the LIMSI, high-speed PIV measurements are performed in an (x, y)-plane, streamwise and normal to the bottom of the cavity, with a frame rate of 500 Hz (figure 4). The velocity field sampling frequency is 250 Hz. The Shannon criterion is satisfied since all frequencies of the flow are typically below 100 Hz. The cavity depth of $D = 50$ mm and the span of $S = 6D$ are fixed. By changing both the cavity length L and the incoming velocity U_0, a wide range of the parameter space is encompassed (table 1). The experimental set-up and datasets are described in detail in Basley *et al.* (2011), Basley (2012) and Basley *et al.* (2013).

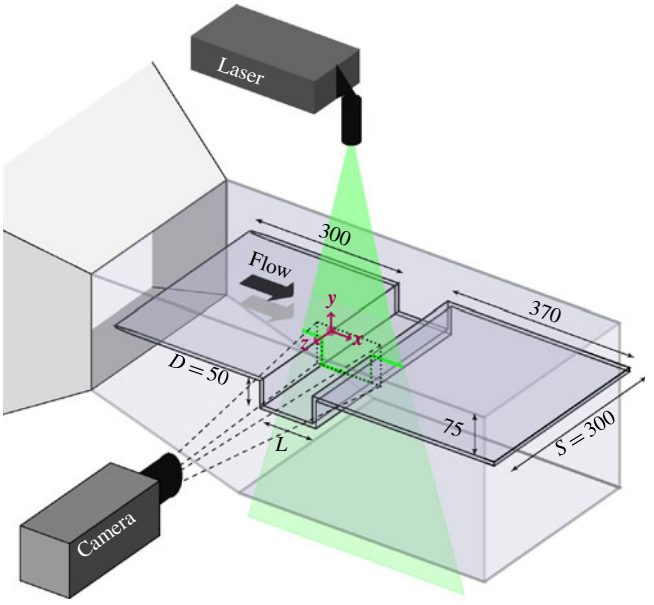

FIGURE 4. (Colour online) Sketch of the experimental set-up used for high-frame-rate PIV measurements in the wind tunnel at LIMSI. The frame of reference is centred in the leading edge at half-span. The cavity length can be varied so that $L/D = \{1.0; 1.5; 1.75; 2.0\}$. TRPIV is performed in an (x, y)-plane (normal to the bottom of the cavity) at $z = -0.4\,D$.

2.2. *High-resolution PIV in a spanwise plane*

The experiments conducted at the LTRAC aim at identifying the spanwise dynamics of the flow. Details can be found in Basley (2012) and de Vicente *et al.* (2014). The results consist of high-resolution PIV data of a (z, x)-plane, parallel to the bottom of the cavity at $y/D = -0.1$ (figure 5). The cavity depth $D = 50$ mm is unchanged and L/D is set to 2. The cavity span, $S = 10\,D$, is larger than that of the LIMSI experiments, so as to better identify spanwise wavelengths. However, it is worth remarking that in both cases the spanwise extension is large enough to ensure that the mean flow is primarily two-dimensional, with the influence of the endwalls remaining secondary to the intrinsic stability properties of the recirculating inner flow. Particle images are recorded by three synchronised 4904 × 3280 px cameras, then are processed by an advanced cross-correlation algorithm (Soria 1996, 1998; Soria, Cater & Kostas 1999). The resulting velocity fields (164 × 823 vectors) are obtained through data merging.

The two investigated cases $Re_D = \{1500; 2400\}$ correspond to low incoming velocities U_0 in water, as reported in table 1. As a result, the two dimensionless sampling frequencies $f_s D/U_0 = \{0.57, 0.39\}$ fully satisfy the Shannon criterion with regards to spanwise dynamics of the inner flow (expression (1.3)) in spite of the low repetition rate – the time interval between velocity fields is typically 3 s. Regarding the shear layer oscillations, control parameters such that $L/\theta_0 \leqslant 60$ imply that the first locked-on mode ($n = 1$) is selected (Sarohia 1977; Basley *et al.* 2013). In other words, the shear layer experiences only one cycle of oscillation within the cavity length L, corresponding to the wavelength $\lambda_{n=1} \sim L$. The associated frequencies are

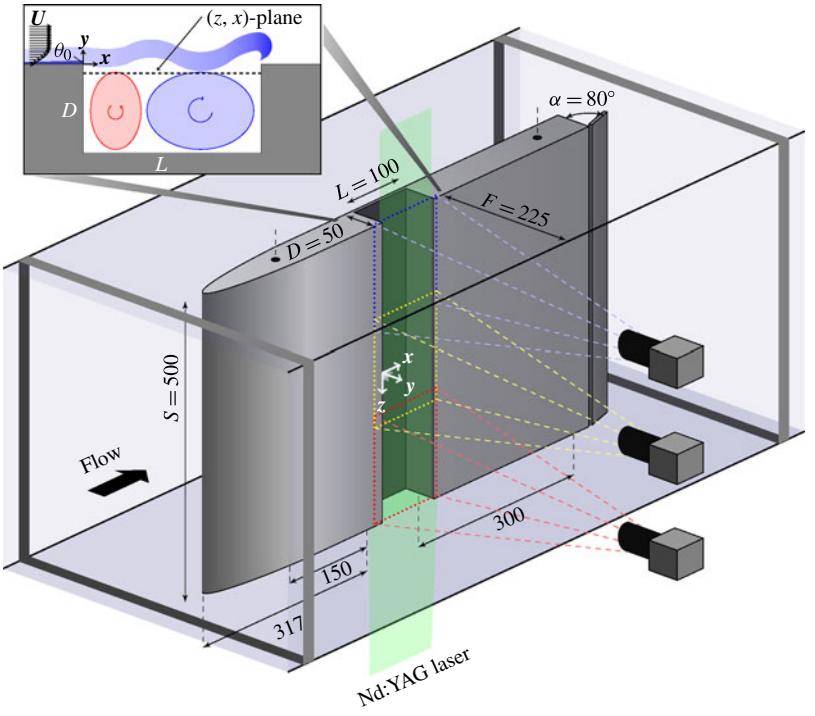

FIGURE 5. (Colour online) The experimental set-up used for high-resolution PIV measurements in the water tunnel at LTRAC. Time-resolved PIV is performed in a (z, x)-plane (spanwise) at $y = -0.1\,D$.

thus $f_{n=1}\,L/U_0 \sim 0.5$ – see (1.1) – and the corresponding Strouhal number based on D is $f_{n=1}\,D/U_0 \sim 0.25$. As reported in table 1, the first case ($Re_D = 1500$, $L/\theta_0 = 46$) is sampled at $f_s\,D/U_0 = 0.57$, making the shear layer oscillations time-resolved. On the other hand, the second investigated case ($Re_D = 2400$, $L/\theta_0 = 59$) is sampled at $f_s\,D/U_0 = 0.39$. This results in aliasing the shear layer oscillations at the apparent frequency $(f_s - f_{n=1})\,D/U_0 \sim 0.39 - 0.25 \sim 0.14$. It should be noted, however, that such an aliasing has limited damage since it does not overlap with other frequencies of the flow.

3. Spectral signature and AM

This section focuses on characterising the slowest dynamics of the flow, in relation to the severe modulations of the shear layer waves. The very low frequencies are identified in power spectra of velocity fluctuations. Their nonlinear interactions with the shear layer oscillations are then revealed using bicoherence.

3.1. *The lowest frequencies of the flow*

Although shear layer vortex shedding constitutes the most salient phenomenon of open cavity flows, high energy is also typically observed for low frequencies in the spectrum. This signature is notably exhibited by time series of velocity fluctuations, as illustrated by figure 6. The power spectra are obtained using the window-averaging method (Welch 1967) out of TRPIV data from the LIMSI campaign. One recognises narrow-banded peaks associated with the self-sustained oscillations of the shear layer

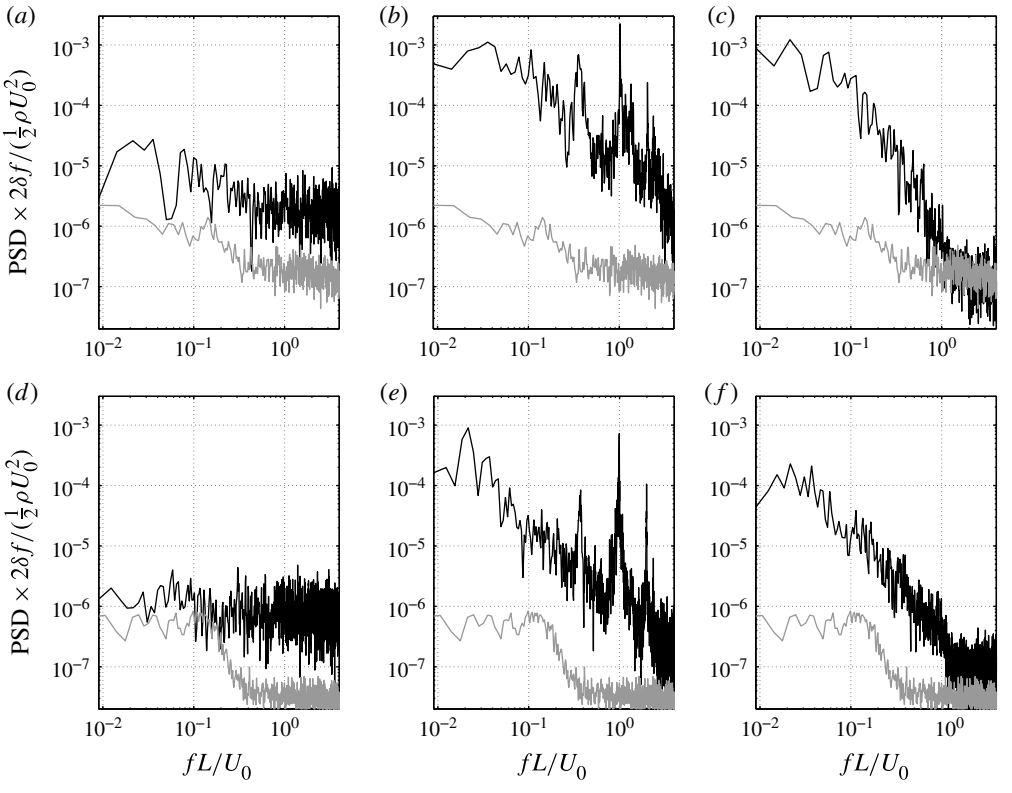

FIGURE 6. Comparative plots of power spectra in the wind tunnel at LIMSI, with δf the frequency step. Streamwise velocity fluctuations are extracted from (x, y)-planar TRPIV datasets at three different locations (black), to be compared with the free stream (gray); that is, when the cavity is removed. Two cases are presented: (*a–c*) $L/D = 2.0$, $U_0 = 1.71$ m s^{-1}, $L/\theta_0 = 91$ and (*d–f*) $L/D = 1.5$, $U_0 = 2.32$ m s^{-1}, $L/\theta_0 = 79$. (*a*) Incoming flow ($x = 0$; $y = 0.4\,D$). (*b*) Shear layer ($x = 1.7\,D$; $y = 0$). (*c*) Inner flow ($x = 0.6\,D$; $y = -0.8\,D$). (*d*) Incoming flow ($x = 0$; $y = 0.4\,D$). (*e*) Shear layer ($x = 1.4\,D$; $y = 0$). (*f*) Inner flow ($x = 1.1\,D$; $y = -0.9\,D$).

in figure 6(*b,e*). However, another range of much lower frequency spikes becomes apparent as the only salient feature of the spectrum inside the cavity (figure 6*c,f*). Indeed, the lowest frequencies of the spectrum have often been disregarded as they can correspond to fluctuations of the upstream flow inherent to experimental facilities. In order to rule out any effect due to forcing of disturbances in the incoming flow, figure 6 compares normalised spectra of an open cavity flow (black curves) with the spectrum in the absence of the cavity (gray curve). The results demonstrate that the free stream exhibits energy levels far lower than those of the cavity flow: about three orders of magnitude with respect to the noticeable peaks of the spectrum, both within the shear layer and inside the cavity. One also notes that there is no correspondence between the highest energy levels of the free stream and any of the peaks observed in the spectra of the flow. The low frequencies spiking in the spectra of figure 6 can only be attributed to the intrinsic dynamics of the open cavity flow.

Such a highly energetic low-frequency range is in fact commonly encountered for all investigated cases. To support this assertion, streamwise laser Doppler velocimetry (LDV) measurements were performed for various control parameters. Time series were

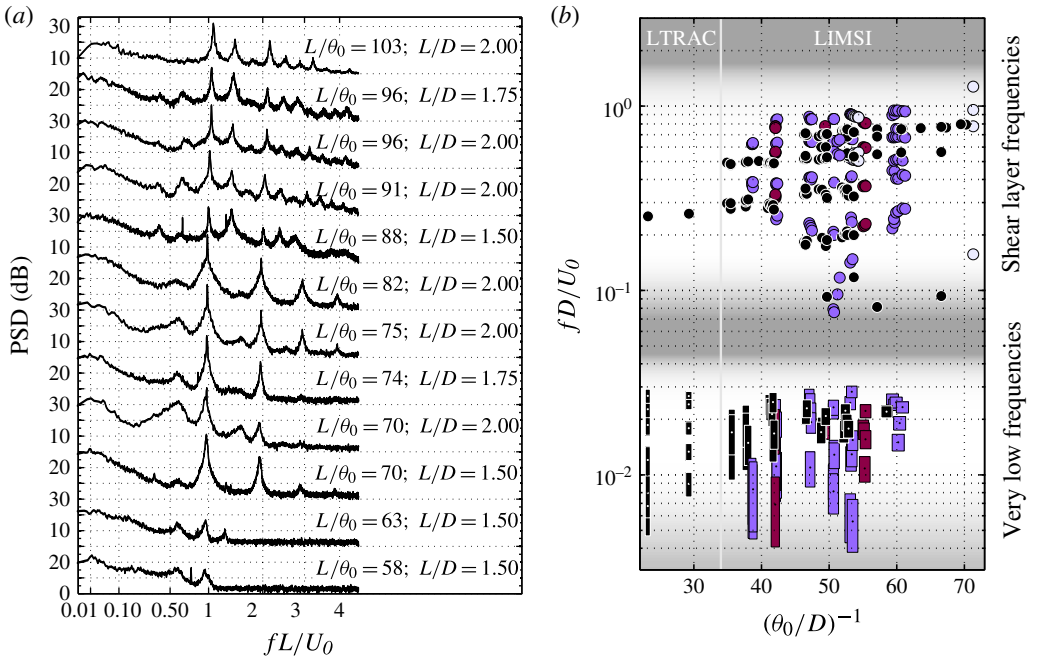

FIGURE 7. (Colour online) Spectral signature of the flow throughout the parameter space. (*a*) Power spectral densities are computed out of streamwise LDV measurements $u'(t)$ in the impinging shear layer, at $(x_{ldv}, y_{ldv}) \simeq (0.95\,L, 0.1\,D)$. For the sake of clarity, each curve is incremented by 30 dB. It should be noted that the curve thickness represents the 95 % confidence interval. (*b*) Dominant frequencies of the flow are extracted out of both LDV and TRPIV data from both LIMSI and LTRAC campaigns (see the text for more details): D-based Strouhal numbers corresponding to most energetic local maxima are plotted against $(\theta_0/D)^{-1}$ for, from light to dark symbols, $L/D = 1$, $L/D = 1.5$, $L/D = 1.75$, $L/D = 2$.

acquired near the impingement over 3 min, i.e. ∼4000 shear layer cycles. Details are given in Basley *et al.* (2011, 2013). The resulting power spectral densities are plotted in figure 7(*a*). On top of the narrow-peaked frequencies of the shear layer, scaling on L, the spectra consistently exhibit a broad-band component at very low frequencies. As mentioned in the introduction, the occurrence of very-low-frequency peaks has been reported in earlier works, but the nature of the underlying physics remains unclear.

3.2. *Two scales in the spectrum*

In order to identify the source of these broad-banded low frequencies and their interactions with the shear layer, space-extended data are required to observe the associated dynamics wherever it is the most energetic. That is the reason why figure 7(*b*) uses TRPIV data to complete the LDV measurements. The use of TRPIV time series allows us to extract time spectra throughout the flow. The spectrum can hence be integrated in space to determine unambiguously the most significant frequencies. This is particularly useful when dealing with broad-banded signatures such as the very low frequencies discussed herein. The results of this analysis are presented in figure 7(*b*), which reports the salient frequencies of the flow within the parameter space. It should be noted that the shear layer frequency $f\,DU_0 = 0.245$

reported for $(\theta_0/D)^{-1} = 29.6$ (LTRAC campaign) has been dealiased, as explained in the previous section. The diagram reveals that the spectral signature consistently splits into two distinct time scales.

The first scale – $f D/U_0 \gtrsim 0.2$ – classically corresponds to fast dynamics dominated by the self-sustained oscillations of the shear layer. These frequencies are primarily associated with locked-on cycles of vortex shedding. The shear layer dynamics also often entails edge frequencies: secondary peaks related to AMs at the impingement. Other works by the authors (Pastur *et al.* 2005; Lusseyran, Pastur & Letellier 2008; Basley *et al.* 2011, 2013) were devoted to these AMs of the impinging shear layer. For instance, one may remark that several frequencies are sensibly lower than the typical shear layer frequencies, basically around $f D/U_0 \sim 0.1$. These spectral components departing from the rest were specifically treated in Basley *et al.* (2013). The reader may refer to the extensive literature concerning shear layer locked-on waves for greater detail, but the present study aims at far lower modulating frequencies, as introduced in § 1.1.

The second scale represents broad-banded slow dynamics and is far less documented. It consists of scattered frequencies such that $0.005 \lesssim f D/U_0 \lesssim 0.04$, for which no simple pattern can be deduced. It should be noted that only the most energetic and statistically pertinent peaks of the low-frequency range are reported. Low-presence-rate components and FFT-induced noise are removed using window-averaging (Welch 1967) and confidence intervals are estimated by χ-functions. If no clear local maximum can be found (even in the inner flow), no frequency is reported. Unlike shear layer waves, the very low frequencies do not scale on L since no separation appears between different L/D ratios. On the other hand, frequencies such that $f D/U_0 \sim 0.02$ are consistent with centrifugal instabilities (expression (1.3)). In the following, Strouhal numbers are always based on the cavity depth D.

3.3. *Modulating frequencies in the inner flow*

The separation of the dynamics into the two aforementioned scales can also be illustrated by the spatial evolution of the spectrum throughout the (x, y)-plane, using the two-component two-dimensional velocity field

$$\boldsymbol{U}(\boldsymbol{x}, t) = [\overline{u}(\boldsymbol{x}) + u'(\boldsymbol{x}, t)]\boldsymbol{e}_x + [\overline{v}(\boldsymbol{x}) + v'(\boldsymbol{x}, t)]\boldsymbol{e}_y, \tag{3.1}$$

where $\{\overline{u}, \overline{v}\}$ are the streamwise and crosswise mean velocities and $\{u'(t), v'(t)\}$ are the streamwise and crosswise velocity fluctuations, at the point $\boldsymbol{x} = (x, y)$. Velocity time series can hereby be extracted from any location in the flow. Figure 8 presents two time series extracted at the impingement and near the bottom of the cavity, respectively, for parameters $L/\theta_0 = 82$, $L/D = 2$, $Re_D = 4550$.

The velocity fluctuations measured at the bottom of the cavity (black curves) are basically free of shear layer waves. The spectral signature is restricted to the low-frequency range, with a broad-banded peak more than 30 dB higher than the rest of the spectrum. More specifically, the spectrum reaches its maximum at a frequency denoted f_Δ, such that $St_\Delta = f_\Delta D/U_0 = 0.024$. This signature suggests that the source of low frequencies lies within the inner flow rather than in the shear layer.

In contrast, the crosswise velocity fluctuations near the impingement (grey curves) predominantly reflect the self-sustained oscillations of the shear layer. The associated power spectrum indeed shows the locked-on frequency f_a, such that $St_a = f_a D/U_0 = 0.49$, and its harmonics $2f_a$, $3f_a$. However, we assert that the low frequencies are indirectly present through the sideband peaks denoted $f_a \pm f_\Delta$. The appearance of combination frequencies $f_a \pm f_\Delta$ is the signature of the AM of a carrier wave at the

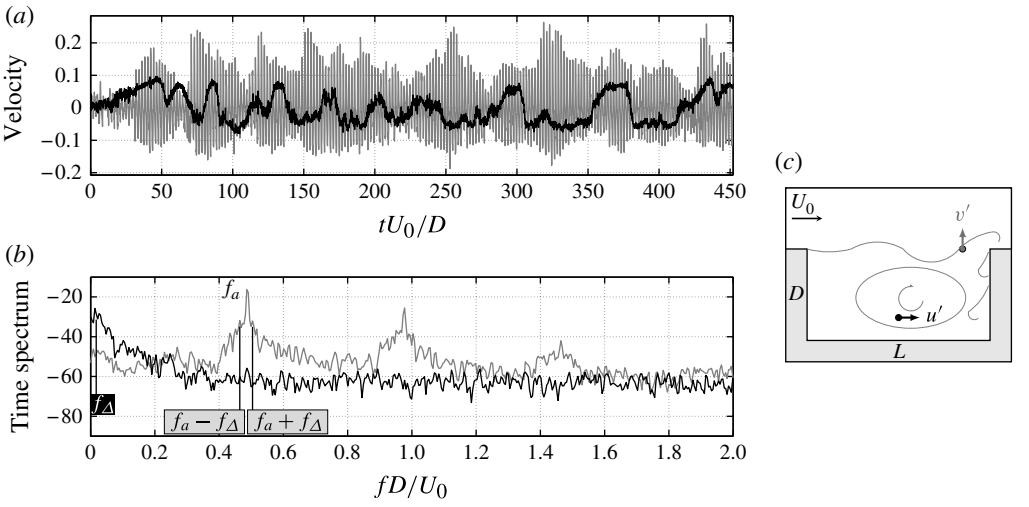

FIGURE 8. Velocity fluctuations extracted from TRPIV datasets for $L/D = 2.0$, $L/\theta_0 = 82$ (LIMSI campaign); gray, $v'(1.70\,D, 0, t)/U_0$; black, $u'(D, -0.75\,D, t)/U_0$. (*a*) Time series are plotted along with (*b*) the associated power spectra (window averaged). (*c*) A sketch of the extraction points in the (x, y)-plane.

frequency f_a by a modulating signal, entailing the frequency f_Δ. In terms of flow dynamics, linear combinations of frequencies in the Fourier space correspond to nonlinear interactions in the physical space: the frequencies $f_a \pm f_\Delta$ indicate quadratic nonlinearities coupling the dynamics associated with f_a (shear layer oscillations) to a second phenomenon associated with the broad-banded peak around f_Δ.

The third-order spectrum, also known as the bispectrum, enables independent spectral components to be distinguished from nonlinearly coupled modes (Kim *et al.* 1980). This tool has been applied to the study of open cavity flows on many occasions, from Knisely & Rockwell (1982) and Isaacson & Marshall (1983) to Larchevêque *et al.* (2004) and Gloerfelt (2006), but only a handful of works have focused the high-order spectral analysis on very low frequencies. Kegerise *et al.* (2004) and recently Vikramaditya & Kurian (2012) highlighted the occurrence of nonlinear interactions between such low frequencies and the dominant frequencies of the shear layer in the compressible regime. The bispectrum of a temporal signal $x(t)$ is the two-dimensional Fourier transform of the third-order cumulant, which is also written as

$$B_{xxx}(f_1, f_2) = \mathrm{E}\left[X(f_1)\,X(f_2)\,X^*(f_1 + f_2)\right], \tag{3.2}$$

where E[.] represents the expectation value, $X(f)$ is the Fourier transform of $x(t)$ and * denotes the complex conjugate. The bispectrum quantifies the energy exchanges within a triad of waves $\{f_1, f_2, f_1 + f_2\}$. More precisely, a non-zero value of $B_{xxx}(f_1, f_2)$ implies that f_1 and f_2 waves transfer energy to the third frequency $f_1 + f_2$ through quadratic nonlinearities. The bispectrum is often normalised by the power spectrum $P_{xx}(f)$ to obtain the bicoherence:

$$b^2_{xxx}(f_1, f_2) = \frac{|B_{xxx}(f_1, f_2)|^2}{P_{xx}(f_1)\,P_{xx}(f_2)\,P_{xx}(f_1 + f_2)}. \tag{3.3}$$

Fourier transform symmetry and the commutativity of expressions (3.2) and (3.3) imply redundancies so that the bispectrum can be fully represented with a triangular

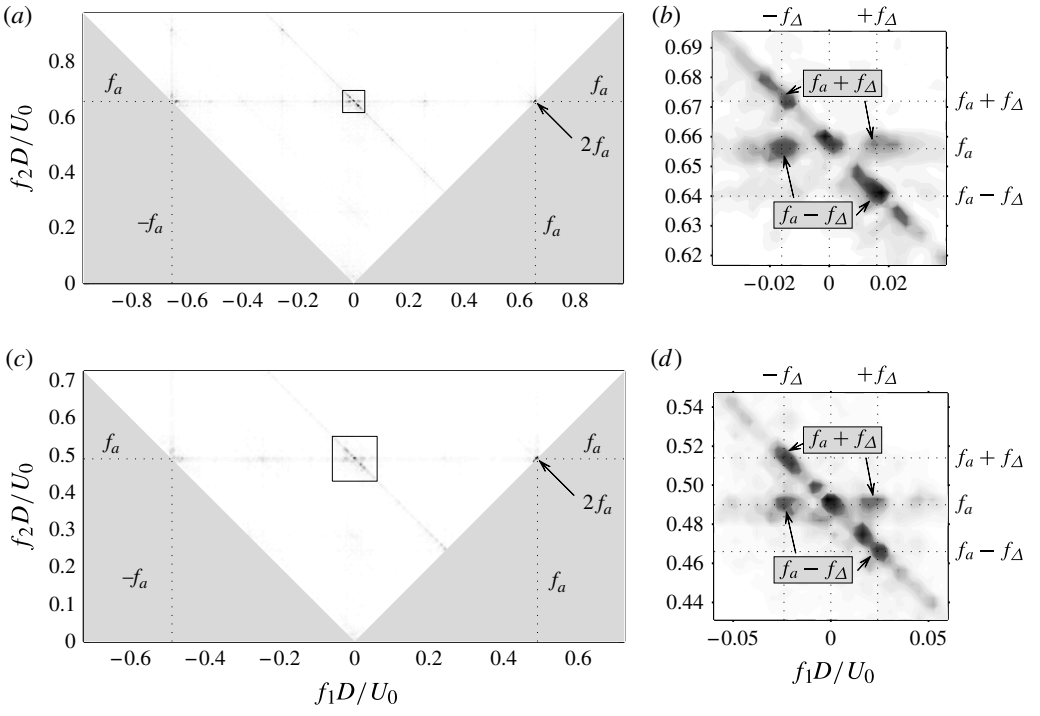

FIGURE 9. Bicoherence computed out of time series of vorticity fluctuations for two cases (LIMSI): (*a,b*) $L/\theta_0 = 79$, $L/D = 1.5$ and (*c,d*) $L/\theta_0 = 82$, $L/D = 2$. The bispectrum is integrated over space near the impingement along the cavity wall ($L - 0.15\,D \leqslant x \leqslant L$, $-0.25\,D \leqslant y \leqslant -0.05\,D$). Panels (*b,d*) show close-ups of the nonlinearities between the two frequencies f_a and f_Δ.

domain. The bicoherence diagrams presented in figure 9 confirm the existence of the nonlinearities hypothesised earlier. For different control parameters, the dominant locked-on frequency, denoted f_a, interacts nonlinearly with the very low frequencies, around f_Δ. As expected, one also observes that the nonlinear saturation of the wave at f_a conveys energy towards the harmonic $2f_a$ through the coupling $\{f_a, f_a\}$. The characteristics of the coupling mechanism between shear layer waves and slow dynamics of the inner flow are addressed further in § 5. Prior to that, the study focuses on identifying the spatial dynamics associated with the broad-band low frequencies.

4. Space–time dynamics of the three-dimensional flow

This section makes extensive use of modal decompositions in both space and time to associate each feature of the spectral signature with its underlying spatial structures. The analysis is first conducted in the plane (x, y) to deal with the dominant dynamics of the flow (§ 4.1). The spanwise extension of the flow is then investigated using the plane (z, x) so as to characterise the three-dimensional waves resulting from centrifugal instabilities (§ 4.2).

4.1. *Space–time decomposition in an (x, y)-plane*

The spatial structures associated with the two aforementioned scales – shear layer modes and very low frequencies – are investigated through proper orthogonal

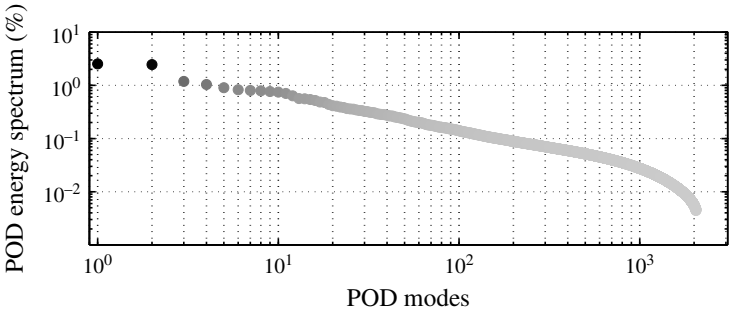

FIGURE 10. Proper orthogonal decomposition eigenvalues, out of TRPIV data for $L/D = 2.0$, $L/\theta_0 = 82$ in an (x, y)-plane; 2048 modes are computed using vorticity fluctuations $\omega_z' D/U_0$.

decomposition (POD), which is commonly used to extract the most coherent structures of the flow. The detail and generalities about the methodology are not the subject here, but the reader may find helpful information, for instance, in Holmes, Lumley & Berkooz (1996) and Cordier & Bergmann (2003). For examples of POD applications and developments in fluid mechanics, one may notably refer to the recent works of Iungo & Lombardi (2011), Kitsios *et al.* (2011), Buchmann, Atkinson & Soria (2013), Cammilleri *et al.* (2013) and Guéniat *et al.* (2014). In the present case, the decomposition is applied to the vorticity fields

$$\omega_z(\boldsymbol{x}, t) = \overline{\omega_z}(\boldsymbol{x}) + \omega_z'(\boldsymbol{x}, t), \tag{4.1}$$

issued from the same (x, y)-plane TRPIV measurements as in the previous section (§ 3.3). Proper orthogonal decomposition is performed on vorticity fluctuations $\omega_z'(\boldsymbol{x}, t)$. In brief, the dataset is contained in a single matrix such that snapshots are successively stacked along rows while columns correspond to time series at every point of the field. By applying singular value decomposition to such a matrix, one splits up space and time dynamics into orthogonal modes associating spatial structures with time series. The decomposition leads to the eigenvalues plotted in figure 10. After the first two equally energetic modes, eigenvalues are significantly lower and decrease smoothly. Several examples among the most salient modes are displayed in figures 11 and 12 for shear layer and inner-flow dynamics, respectively.

The first two (most energetic) modes represent the dominant shear layer wave, see figure 11 (top). The spatial structure of mode 1 exhibits a locked-on mode consisting of two cycles of vortices shed along L. Temporally, mode 1 is restricted to the single narrow-peaked frequency at $St_a = 0.49$. Mode 2 is in quadrature of phase to mode 1, which denotes a travelling wave. Shear layer dynamics then reappears in mode 7, see figure 11 (bottom). Along with mode 8 in quadrature, they convey a fast travelling wave characteristic of the first harmonic to the dominant shear layer wave (mode 1). As such, the streamwise wavelength entailed by mode 7 is half that of mode 1 and the time power spectrum peaks at the frequency $St_{a2} = 0.98 = 2\,St_a$. These POD modes are perfectly consistent with other POD studies from the literature on cavity flows (Rowley, Colonius & Murray 2000; Podvin *et al.* 2006; Gloerfelt 2008). One may also notice the similarity with global Fourier modes obtained in Rowley, Colonius & Basu (2002), Basley *et al.* (2011) and Basley *et al.* (2013). It is worth highlighting that AM by very low frequencies is recovered in both shear layer waves. One remarks notably the sideband peaks $St_a \pm St_\Delta$ in the time spectrum of mode 7.

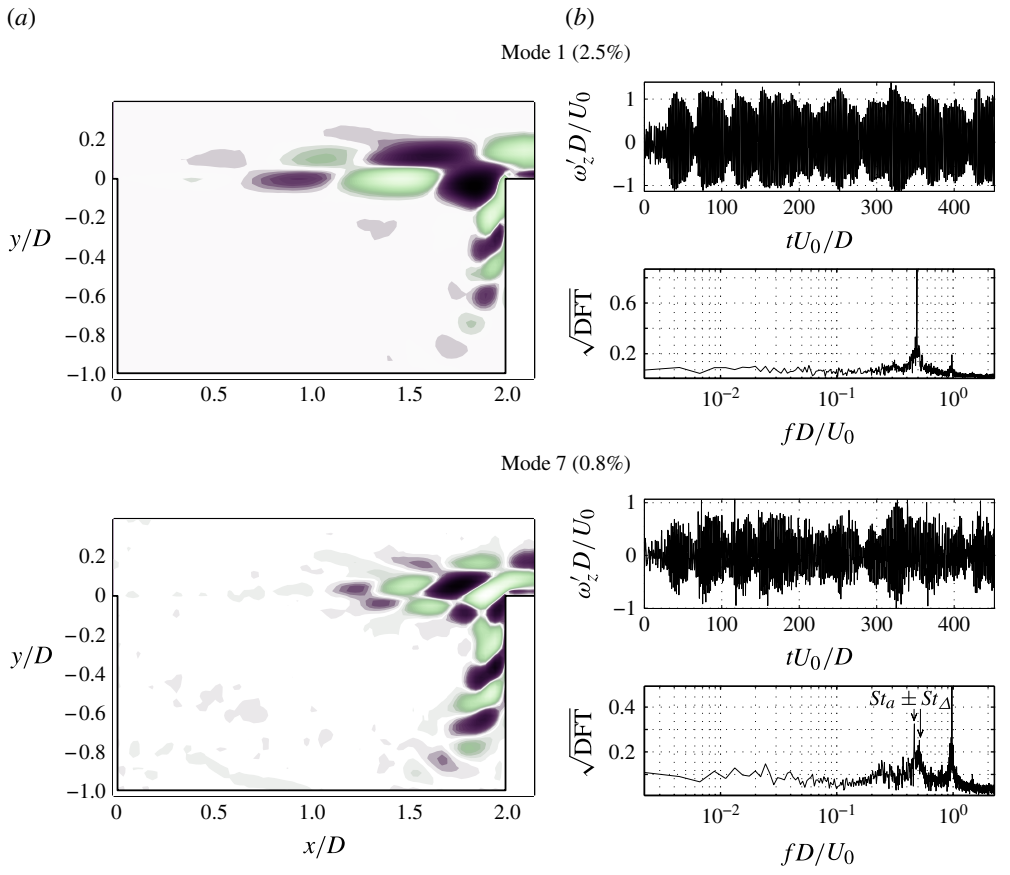

FIGURE 11. (Colour online) Proper orthogonal decomposition modes representing shear layer dynamics, out of TRPIV data for $L/D = 2.0$, $L/\theta_0 = 82$ in an (x, y)-plane. Spatial modes (a) are associated with temporal modes (b) plotted as both time series and amplitude spectra.

The slow dynamics of the inner flow is first observed in mode 3, see figure 12. The spatial structures depict large-scale fluctuations carried by the main recirculation and the associated temporal features recover the broad-banded low frequencies peaking at $St_\Delta = 0.024$ with a secondary peak at $St = 0.041$. Modes 4 and 5 exhibit similar dynamics. These modes do not represent streamwise travelling eddies but rather organise as layers of alternate shear vorticity wrapped around the main recirculation. This organisation denotes non-negligible out-of-plane fluctuations. Furthermore, one may notice that the signature is particularly intense within the centrifugally unstable regions – earlier revealed in figure 3 – suggesting three-dimensional dynamics. The three-dimensionality of this slow dynamics is also demonstrated by its absence in 2D simulations. For instance, the salient POD modes reported in Rowley *et al.* (2000), Gloerfelt (2006) and Gloerfelt (2008) exclusively reflect shear layer waves. On the other hand, the 3D numerical study conducted in Podvin *et al.* (2006) showed similar slow dynamics, actually connected to spanwise oscillations inside the cavity. The latter modes can be compared with results from global Fourier decomposition to bring further insight. Recently, the experimental investigation in Basley *et al.* (2013) used global Fourier modes to identify the low-frequency dynamics in a flow

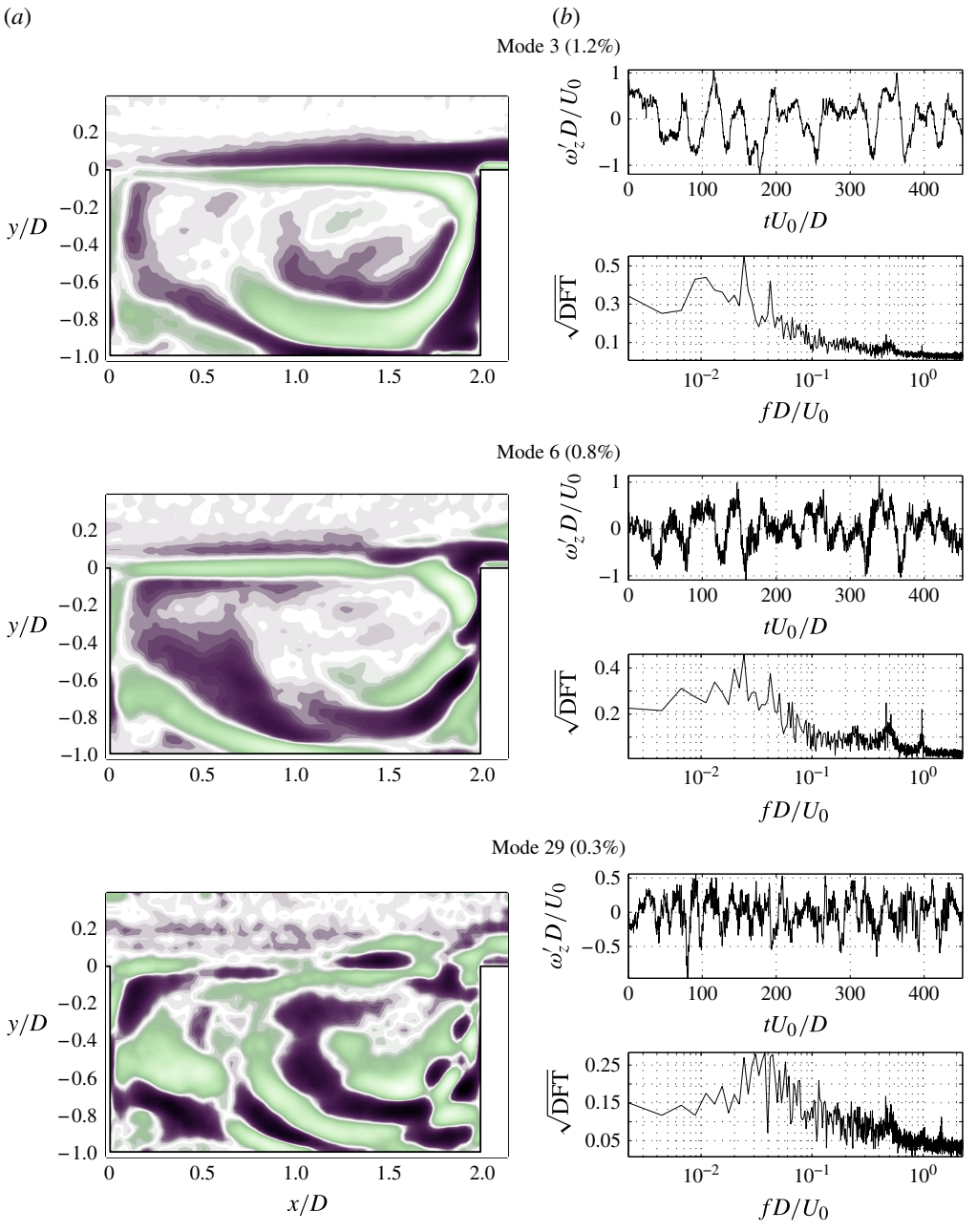

FIGURE 12. (Colour online) POD modes representing inner flow slow dynamics, out of TRPIV data for $L/D = 2.0$, $L/\theta_0 = 82$ in an (x, y)-plane. Spatial modes (a) are associated with temporal modes (b) plotted as both time series and amplitude spectra.

presenting an unusual multi-modulated signature. The extensive study was focused on a single configuration ($L/D = 1.5$, $L/\theta_0 = 76$). The dynamics associated with a very-low-frequency $f_\Delta D/U_0 \simeq 0.02$ was consistent with figure 12 and involved spanwise variations.

The present results as well as previous works point to centrifugal instabilities arising along the main recirculation. Such a spatio-temporal signature would result from three-dimensional waves described notably in Brès & Colonius (2008), de Vicente *et al.* (2014) and Meseguer-Garrido *et al.* (2014). Three-dimensional eddies winding around the main vortex, confined in the outer regions along the walls, would travel spanwise across the (x, y)-plane.

The rest of the modes do not strictly represent either inner-flow dynamics or shear layer oscillations. Both temporal and spatial modes involve fast-moving structures related to slower events. For instance, modes 6 and 29 – in figure 12 – mix the energetic broad-banded signature of slow dynamics around the main recirculation with features reminiscent of shear layer oscillations. More specifically, the time spectrum associated with mode 6 highlights the broad-banded low frequencies and the shear layer frequency $St_{a2} \simeq 1.0$. For mode 29, the shear layer dynamics is present through the second harmonic at $St_{a3} \simeq 1.5$. Of particular interest is the recurring presence of the sideband peaks $St_a \pm St_\Delta$, denoting the AM by St_Δ. This coherence of the slow dynamics inside the cavity with amplitude-modulated fast dynamics of the shear layer confirms the importance of nonlinear interactions between the two phenomena.

4.2. *Space–time decomposition in a (z, x)-plane*

The focus is now on the spanwise extension of the flow to investigate the three-dimensional dynamics at play inside the cavity. The subsequent analysis is based on TRPIV measurements performed in a (z, x)-plane spanning the cavity at $y = -0.1\,D$ for $Re_D = 2400$, $L/\theta_0 = 59$, $\theta_0/D = 0.034$, $L/D = 2$ for the experiments described in § 2.2. Since the recordings are time-resolved, space–time decomposition can be used to identify the spanwise dynamics associated with the characteristic frequencies. In a previous study (de Vicente *et al.* 2014) the analysis was conducted using global Fourier decomposition of crosswise vorticity fluctuations ω_y'. The saturated three-dimensional dynamics was characterised with regards to the onset of centrifugal instabilities along the recirculating inner flow. Sets of spanwise-travelling waves were identified in the experiments and the global Fourier modes exhibited patterns that matched locally the eigenmodes that arose from linear stability analysis. As expected, the identified spanwise-travelling waves involved frequencies consistent with centrifugal instabilities (expression (1.3)).

The present investigation aims to relate the spanwise dynamics of the inner flow to AMs of the shear layer waves. The space–time decomposition is achieved using POD applied to the streamwise velocity fluctuations $u'(z, x, y = -0.1\,D, t)$. This plane of study offers an ideal location encompassing the shear layer oscillations as well as the recirculating inner flow.

4.2.1. *Proper orthogonal decomposition and the Hilbert–Huang transform*

Proper orthogonal decomposition eigenvalues are plotted in figure 13. It should be noted that the energy decreases smoothly and that more than two orders of magnitude separate the first from the last of the 365 computed modes. Once spatial and temporal POD modes are obtained, spectral analysis is undertaken to determine the spanwise wavelengths λ_z and Strouhal numbers characterising this flow. Application of a space Fourier transform provides statistical (integrated) information since it relies on a scalar product. Local estimation of the wave properties of the POD modes brings further insight into the modulations of the identified coherent structures (Basley 2012). In that context, the Hilbert–Huang transforms (HHTs) are computed from the POD modes both spanwise and timewise.

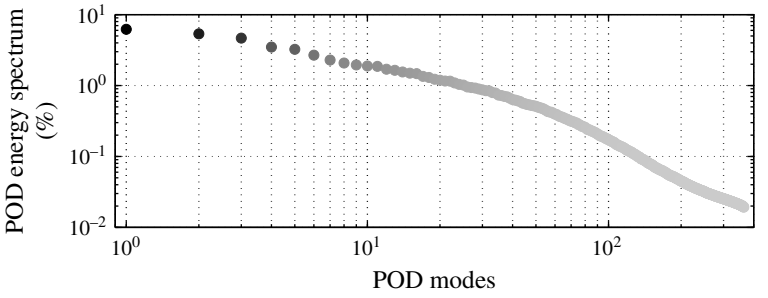

FIGURE 13. Proper orthogonal decomposition eigenvalues out of TRPIV data for $Re_D = 2400$, $L/D = 2.0$, $L/\theta_0 = 59$, $\theta_0/D = 0.034$, in a (z, x)-plane, using streamwise velocity fluctuations u' from 365 snapshots.

Since its development by Huang (Huang, Long & Shen 1996; Huang *et al.* 1998; Huang, Shen & Long 1999), the HHT has been extensively utilised to investigate distorted signals resulting from multi-scale and/or modulated dynamics, in particular, nonlinearly saturated waves which involve a non-constant frequency and where the instantaneous frequency varies over one period of oscillation. In that context, HHT is a powerful tool as it enables the precise identification of the instantaneous frequency. The reader may refer to Basley (2012) for the basics of HHT methodology, and an exhaustive discussion is available in Huang *et al.* (1998). In principle, the HHT uses the empirical mode decomposition (EMD) to extract zero-mean oscillatory functions, on which the classical Hilbert transform is applied. The originality of EMD comes from its model-free *a posteriori*-defined basis. The decomposition relies entirely and directly on the data, without any pre-requirement for the modes resulting from the process. One only assumes that a signal can be decomposed into a set of zero-mean oscillatory modes, referred to as intrinsic mode functions (IMFs). Such functions are obtained by a sifting process, which consists in subtracting from the signal its running average, defined as the local mean value of the inferior and superior envelopes. By applying the same process recursively, the running average eventually tends to zero, with oscillations ending up properly centred. Once an IMF is extracted, the same sifting process is applied to the remaining signal until the residue becomes a constant or contains one oscillation at the most. In brief, an IMF constitutes an oscillating signal, not necessarily sinusoidal, that may involve various length scales and amplitudes but whose mean is always zero. One can thus appreciate that such an oscillatory function can meet the requirements for a Hilbert transform (Pastur *et al.* 2008). Construction of an analytic signal provides the local amplitude and phase of the IMF under consideration. From the phase gradient, the local frequency is estimated, or the local wavenumber if the signal is a function of space. As a result, each IMF provides a Hilbert–Huang spectrum, a function that associates local frequency with local amplitude. In the following, only the most energetic IMF is considered.

4.2.2. *Analysis of the spanwise dynamics*

Prior to analysing the POD modes separately, characteristic wavelengths are estimated using the marginal spectrum of the spatial modes altogether. This marginal spectrum is obtained by integrating the Hilbert–Huang spectrum over z and summing up the contributions from all spanwise rows. The marginal spectrum is plotted in figure 14(*a*). The spanwise spectrum highlights two main wavelengths. The

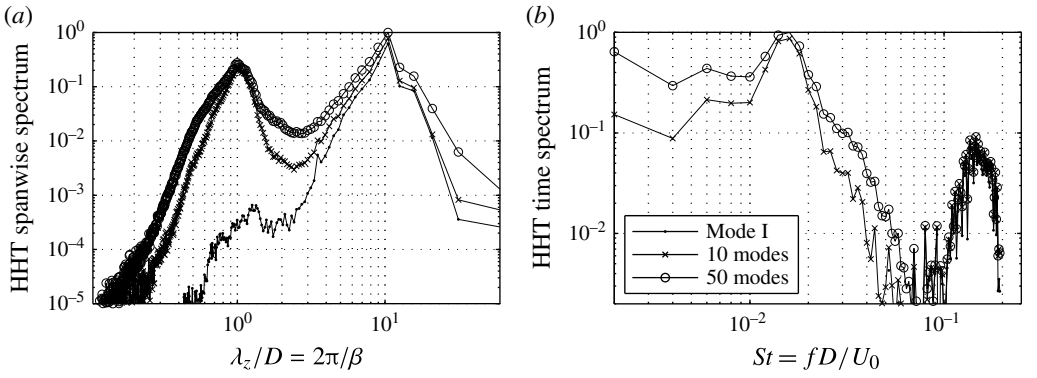

FIGURE 14. Hilbert–Huang marginal spectra for both spatial (a) and temporal (b) POD modes in a (z, x)-plane for $Re_D = 2400$, $L/D = 2.0$, $L/\theta_0 = 59$, $\theta_0/D = 0.034$.

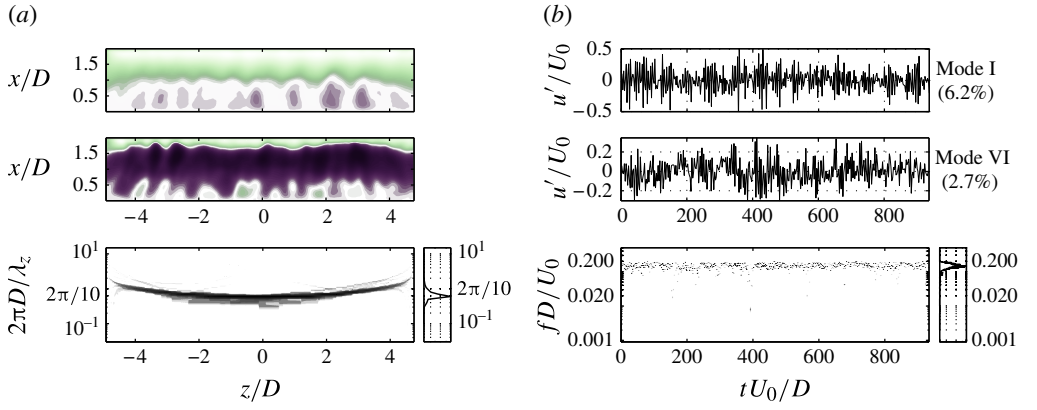

FIGURE 15. (Colour online) Proper orthogonal decomposition modes {I,VI} computed out of TRPIV data for $L/D = 2.0$, $L/\theta_0 = 59$, $\theta_0/D = 0.034$, in the (z, x)-plane ($y = -0.1\,D$). The spatial modes (a) are associated with the temporal modes (b). Homologous POD modes are brought together and analysed using HHT (bottom) to identify locally the associated wavenumbers and frequencies, along with the marginal (integrated) spectra.

first salient wavelength $\lambda_z \simeq 10\,D$ represents the cavity span. This corresponds to quasi-two-dimensional dynamics restricted by the endwalls at $z = \pm 5\,D$. This signature is mostly carried by mode I. The rest of the POD modes exhibit wavelengths around $\lambda_z = D$, which is consistent with patterns generated by centrifugal instabilities.

We proceed similarly to identify characteristic frequencies out of the temporal POD modes. The resulting time marginal spectrum is presented in figure 14(b). It involves the two same characteristic scales, one order of magnitude apart, as pointed out in the previous section (§ 3). The dominant Strouhal number at $f\,D/U_0 \sim 0.015$ represents the very low frequencies implied by the inner flow, while the second salient peak observed around $f\,D/U_0 \sim 0.14$ is likely to correspond to aliased frequencies associated with shear layer oscillations. More insight is available through mode-to-mode analysis of the most energetic POD modes. These are illustrated in figures 15–17 along with the corresponding spanwise and timewise Hilbert–Huang spectra.

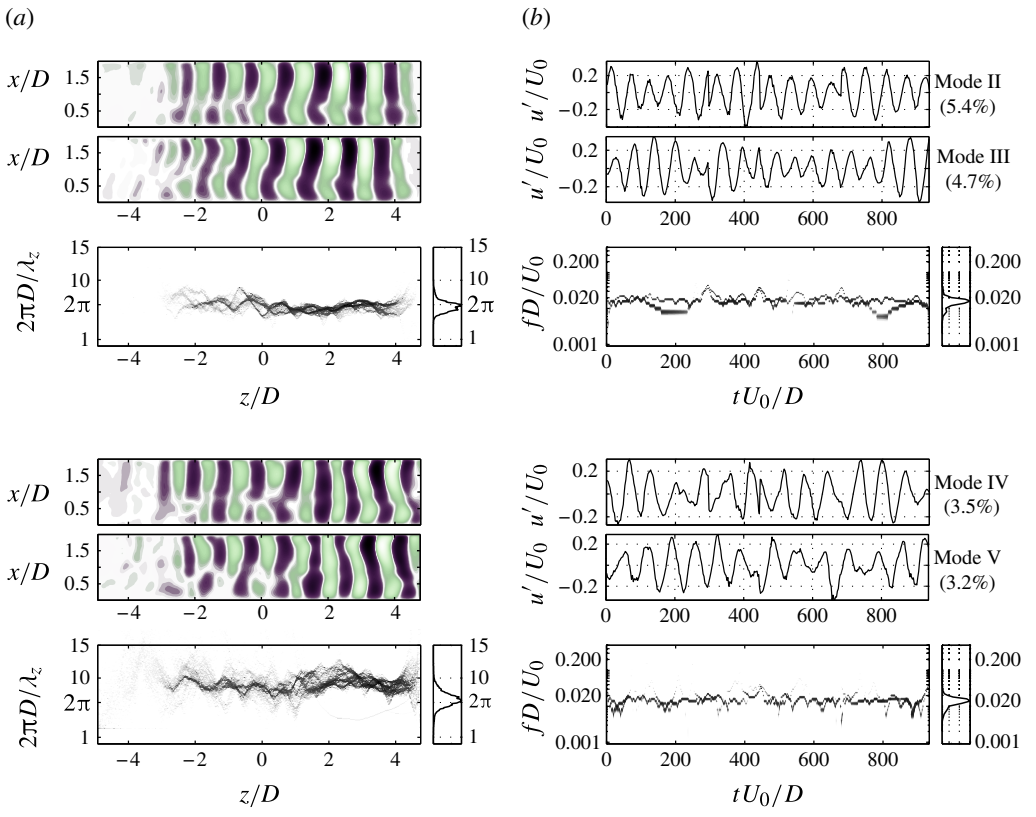

FIGURE 16. (Colour online) Proper orthogonal decomposition modes {II,III} and {IV,V} computed out of TRPIV data for $L/D = 2.0$, $L/\theta_0 = 59$, $\theta_0/D = 0.034$, in the (z, x)-plane ($y = -0.1\,D$). See the caption to figure 15 for more detail.

Modes I and VI recover shear layer vortex shedding, with spatial structures dominated by streamwise-travelling waves spanning the cavity, as seen in figure 15. This pair of modes is characterised by a quasi-constant spanwise wavenumber $\beta = 2\pi D/\lambda_z \simeq 2\pi/10$ ($\lambda_z \simeq 10\,D$), mentioned above with regard to the total marginal HHT spectrum in figure 14. The streamwise wavelength associated with shear layer oscillations can be estimated to be approximately equal to the cavity length, implying one cycle of oscillation ($n = 1$) as expected for a dimensionless cavity length of $L/\theta_0 = 59$. Timewise, such a locked-on mode is associated with a frequency $f_1\,L/U_0 \sim 0.5$ (1.1), that is, $f_1\,D/U_0 \sim 0.25$. With a Nyquist frequency at $f_{Nyq} = f_s/2 = 0.195\ U_0/D$ – see table 1 – such a frequency is aliased at $(2f_{Nyq} - f_1)\,D/U_0 \sim 0.14$, matching precisely the Strouhal numbers identified by HHT from the POD modes.

The primarily two-dimensional organisation of modes I and VI appears superimposed with spanwise oscillations of lower amplitude. These are more visible in the upstream half of the cavity before being overridden by the growing shear layer oscillations. Furthermore, the temporal signature is once again amplitude modulated by very low frequencies around $0.015\,U_0/D$, confirming that this AM occurs consistently for various control parameters.

Modes II, III and IV, V organise as two pairs of homologous patterns in phase quadrature (figure 16). Each pair conveys a highly coherent monochromatic spanwise-

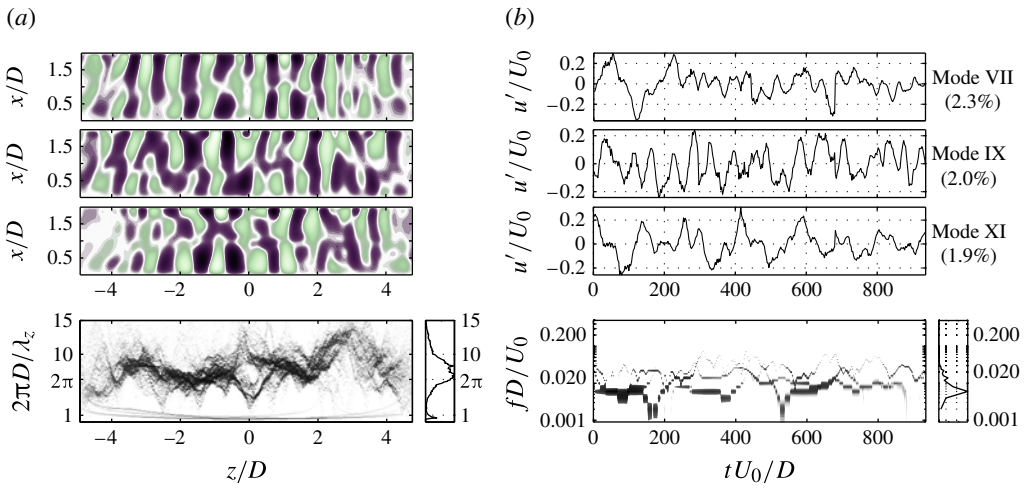

FIGURE 17. (Colour online) Proper orthogonal decomposition modes {VII,IX,XI} computed out of TRPIV data for $L/D = 2.0$, $L/\theta_0 = 59$, $\theta_0/D = 0.034$, in the (z, x)-plane $y = -0.1\,D$. See the caption to figure 15 for more detail.

travelling wave. The well-defined phase fronts are parallel, yet slightly skewed, as they stand for helical structures coiling up the recirculating flow. Modes II and III represent a left-travelling wave associated with, on average, the wavenumber $\beta \approx 2\pi$ and Strouhal number $f\,D/U_0 \approx 0.016$, while modes III and IV depict a right-travelling wave associated with a similar wavenumber and a slightly lower Strouhal number of $f\,D/U_0 \approx 0.014$. For both waves, nonlinear distortion is revealed by wavenumber fluctuations along the span. These saturated spanwise waves of wavelengths $\lambda_z \sim D$ result from centrifugal instabilities onset along the recirculation inside the cavity.

In fact, these two pairs of POD modes entail the same dynamics as the global Fourier modes in Basley (2012) and de Vicente *et al.* (2014). This is fully consistent with other experimental results by Douay *et al.* (2011) and Basley *et al.* (2013): the primary spanwise disturbances of the inner flow are quasi-symmetric counter-propagating spanwise waves. When such counter-propagating waves overlap, their interference leads locally to a (quasi) standing wave (Douay *et al.* 2011; Basley 2012).

It is also important to note the correspondence with the modulating frequency in the time series of modes I and VI, inferring the key role played by the salient spanwise-travelling waves of modes II–V in the drastic AM of the shear layer waves.

From mode VII, all spatial POD modes involve broader-banded dynamics with non-trivial spatial structures. Modes VII, IX and XI are presented in figure 17 as examples of such features. They exhibit multiple patterns distributed over the entire span and characterised by large variations of spanwise wavenumbers in the range $3 \lesssim \beta \lesssim 13$. Consistently, the temporal modes present diverse time scales in the range $0.002 \lesssim f\,D/U_0 \lesssim 0.03$. These POD modes probably participate in the inner-flow dynamics deriving from centrifugal instabilities and modulating the shear layer oscillations.

Until now, the study has focused on identifying and characterising the slow dynamics responsible for the severe AM of the shear layer self-sustained oscillations. The analysis has demonstrated that the very low modulating frequencies are associated with three-dimensional coherent structures resulting from centrifugal instabilities. This dynamics organises as slow-moving spanwise-travelling helical waves which arise

within the inner flow and yield a wavelength $\lambda_z \approx D$. The way in which these three-dimensional waves interact nonlinearly with the shear layer vortex shedding is studied in detail in the next section.

5. Nonlinear coupling with inner-flow 3D waves

The focus of the analysis that follows is now on the coupling mechanism linking inner-flow spanwise waves to shear layer AMs. As shear layer oscillations and centrifugal instabilities evolve over very different time scales, the connection can be investigated by separating the fast from the slow dynamics of the flow.

5.1. *Scale separation*

The flow is split according to the two aforementioned time scales: CI, frequencies consistent with centrifugal instabilities, in the range of expression (1.3); and SL, the locked-on frequencies of the shear layer, verifying (1.1). The latter scale corresponds to carrier frequencies of the amplitude-modulated oscillations. Therefore, it must be demodulated so as to extract the envelope. The envelope is then discussed with regards to the three-dimensional waves inside the cavity so as to characterise the nonlinear interactions between shear layer waves and centrifugal instabilities. Scale separation is utilised in the (x, y)- and (z, x)-planes under investigation to reconstruct the low-frequency dynamics of the inner flow on one hand and the shear layer dynamics on the other hand.

5.1.1. *Proper orthogonal decomposition partial reconstruction in the (z, x)-plane*

Proper orthogonal decomposition avails us to reconstruct part of the dynamics considering only a few relevant modes. The reconstructed space–time dynamics is obtained from

$$R(\boldsymbol{x}, t) = \boldsymbol{U} \times \boldsymbol{S} \times \boldsymbol{V}^{\mathrm{T}}, \tag{5.1}$$

where $\boldsymbol{U}$ and $\boldsymbol{V}$ are the unitary matrices containing respectively the spatial and temporal signatures of the selected POD modes and $\boldsymbol{S}$ is the diagonal matrix containing the associated singular values. In the following, $R_{SL}(z, x, t)$ is the reconstruction using modes {I,VI} corresponding to shear layer dynamics while $R_{CI}(z, x, t)$ uses modes {II–V, VII–XI} so as to contain the dynamics derived from centrifugal instabilities.

5.1.2. *Spectral filtering in the (x, y)-plane*

Unlike the (z, x)-plane, the POD modes computed from the (x, y)-plane – in § 4.1 – do not strictly separate the two time scales. Spectral filtering is here preferred to separate the low-frequency range from the self-sustained oscillations. Butterworth filters of order 4 are applied to the time series throughout the fluctuating fields, as illustrated in figure 18.

First, low-pass filtering is used with a cutoff frequency $f_c D/U_0 = 0.07$, so as to encompass the low-frequency broad-band peak (figure 18*a*) corresponding to the reconstructed dynamics, $R_{CI}(x, y, t)$. The filtered snapshot and root mean square (r.m.s.) distribution in figure 18(*b*,*c*) render the inner-flow dynamics wrapped around the main recirculation characteristic of centrifugal instabilities.

Second, a band-pass filter is applied to remove all time scales apart from the carrier frequency of the self-sustained oscillations. In the example shown in figure 18(*d*), the filtered spectrum only shows significant energy around the (dominant) locked-on frequency – $f_a D/U_0 \simeq 0.5$ in figure 18. As expected, the reconstructed dynamics

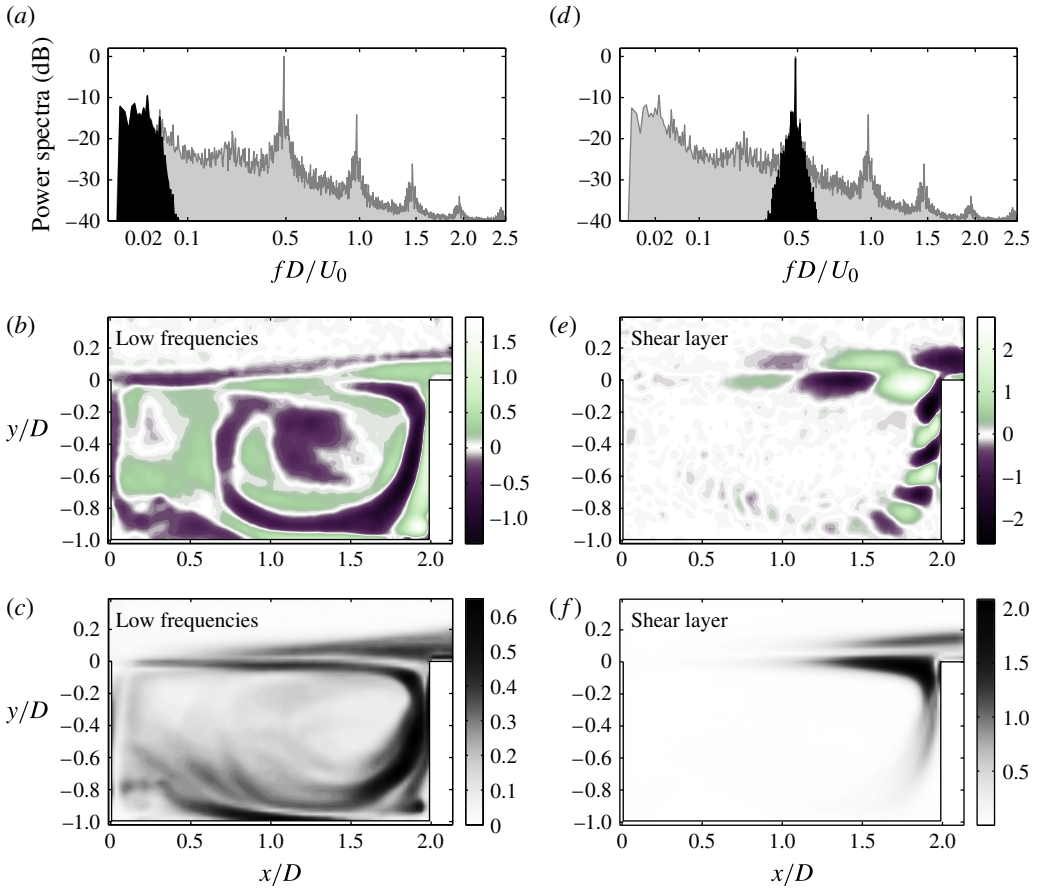

FIGURE 18. (Colour online) Time-filtered vorticity fluctuations in an (x, y)-plane, for $L/D = 2.0$ and $L/\theta_0 = 82$. (*a–c*) Low-pass to keep centrifugal instabilities only, $R_{CI}(x, y, t)$. (*d–f*) Band-pass around the dominant shear layer frequency, $R_{SL}(x, y, t)$. (*a,d*) Power spectra. (*b,e*) Examples of filtered snapshots. (*c,f*) Vorticity r.m.s.

$R_{SL}(x, y, t)$ is restricted to the shear layer flapping motion. The filtered snapshot in figure 18(*e*) depicts shear layer oscillations and, to a lesser extent, inflows along the downstream wall of the cavity. This is confirmed by the high r.m.s. levels in the impingement region, leaving the inner flow basically free of high frequency dynamics (figure 18*f*).

5.2. *Amplitude modulation by spanwise waves*

The AM of the self-sustained oscillations is analysed with respect to the spanwise waves inside the cavity. Cross-correlations are used to ascertain the prominent effect of the inner-flow centrifugal instabilities on the shear layer oscillations throughout the parameter range investigated.

5.2.1. *Envelope of the shear layer waves*

Once the shear layer dynamics is reconstructed in R_{SL}, one obtains an amplitude-modulated signal consisting of a carrier – the locked-on (high) frequency – and

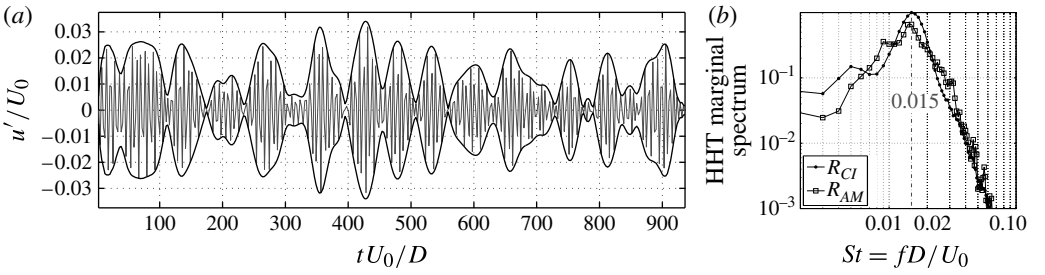

FIGURE 19. Temporal dynamics of the amplitude of the shear layer oscillations for the case $L/\theta_0 = 59$, $L/D = 2$, $Re_D = 2400$. (*a*) Time series $R_{SL}(z = 3\,D, x = 1.84\,D, t)$ extracted from shear layer reconstructed dynamics near the impingement, along with the associated envelope $R_{AM}(z = 3\,D, x = 1.84\,D, t)$. (*b*) Hilbert–Huang marginal (integrated) spectra of both the shear layer envelope R_{AM} and the slow dynamics R_{CI} are confronted.

an envelope. Application of the Hilbert transform to every zero-mean time series extracted across the (z, x)-plane enables us to construct an analytic (complex) signal, whose instantaneous amplitude represents the envelope of the self-sustained oscillations. As this envelope reveals the AM of shear layer oscillations, it will be referred to as $R_{AM}(\boldsymbol{x}, t)$.

The extraction of $R_{AM}(\boldsymbol{x}, t)$ is illustrated in figure 19(*a*) for the case $Re_D = 2400$, $L/\theta_0 = 59$, $L/D = 2$, already investigated in § 4.2. The HHT is applied to the time series of both R_{AM} and R_{CI} in order to obtain the instantaneous dominant frequencies involved in both the shear layer modulations and the slow dynamics. The resulting marginal spectra plotted in figure 19(*b*) are integrated both in the spanwise position and over time. Both R_{AM} and R_{CI} exhibit a unique salient Strouhal number at 0.015. It corresponds to the central frequency of the two counter-travelling spanwise waves – depicted by the POD modes II–V – associated with frequencies of 0.014 and 0.016. The match between the spectral contents of R_{AM} and those of R_{CI} demonstrates once more the prominent influence of inner-flow centrifugal instabilities on the AM.

5.2.2. *Modulating dynamics*

The role of the inner-flow centrifugal instabilities as modulating dynamics of the shear layer waves is consistently recovered for different control parameters. This assertion is notably confirmed by the temporal correlations of the time series resulting from R_{AM} and R_{CI} along the shear layer. Four different parametric cases are presented in figure 20. Salient features are common to all cases despite the increasing complexity with larger control parameters Re_D and L/θ_0. The auto-correlation of both R_{CI} and R_{AM} consistently depicts a fairly periodic signature involving similar time scales, see figure 20(*a–d*) (top, middle). As expected, the associated frequencies are characteristic of centrifugal instabilities (1.3). Even more remarkable are the high correlation levels in $R_{CI} \star R_{AM}$ – see figure 20(*a–d*) (bottom) – even over large time horizons. These high cross-correlations corroborate the close connection between inner-flow centrifugal instabilities and the modulated dynamics of the shear layer waves.

Nevertheless, modulating and modulated dynamics evolve slightly differently throughout the parameter space. The case shown in figure 20(*a*) presents a large spanwise extension and a small dimensionless cavity length L/θ_0. The reconstructed dynamics R_{CI} is highly coherent and uniformly correlated along the cavity length. The spanwise waves derived from centrifugal instabilities hereby prevail over the

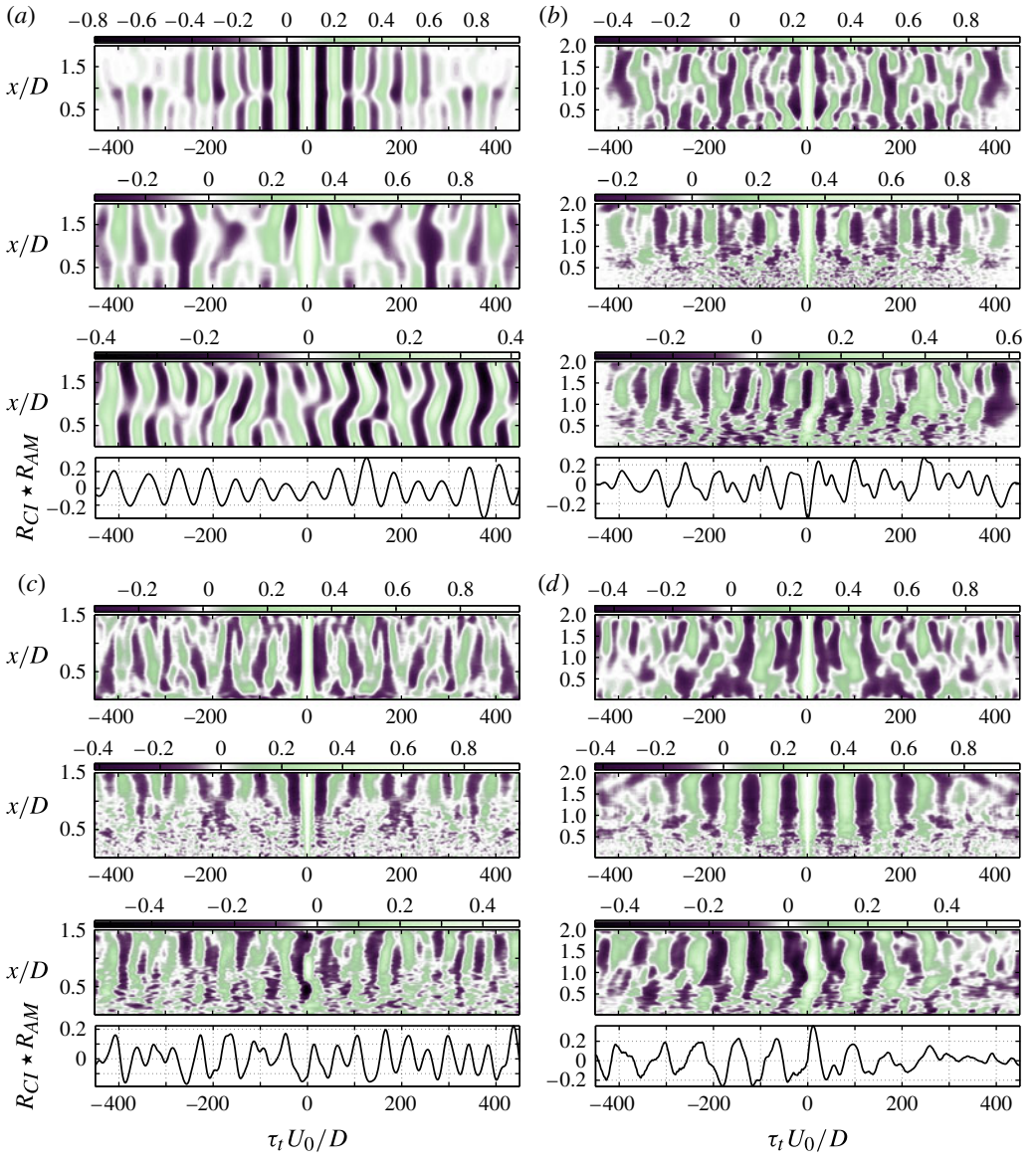

FIGURE 20. (Colour online) Time cross-correlations computed from streamwise velocity fluctuations u'/U_0 along x at $y = -0.1\,D$ close to mid-span in the reconstructed dynamics R_{CI} and R_{AM}, for four experimental cases. For each case and from top to bottom, auto-correlation $R_{CI}(x, t) \star R_{CI}(x, t)$, auto-correlation $R_{AM}(x, t) \star R_{AM}(x, t)$, cross-correlation $R_{CI}(x, t) \star R_{AM}(x, t)$ and extraction $R_{CI}(x = 0.75\,L, t) \star R_{AM}(x = 0.75\,L, t)$. (*a*) $Re_D = 2400$, $L/\theta_0 = 59$, $L/D = 2$, $S/D = 10$. (*b*) $Re_D = 4550$, $L/\theta_0 = 82$, $L/D = 2$, $S/D = 6$. (*c*) $Re_D = 7470$, $L/\theta_0 = 79$, $L/D = 1.5$, $S/D = 6$. (*d*) $Re_D = 5750$, $L/\theta_0 = 91$, $L/D = 2$, $S/D = 6$.

modulated dynamics of the shear layer R_{AM}. In contrast, the case seen in figure 20(*d*) corresponds to a higher Reynolds number and a higher dimensionless cavity length, with a smaller cavity span. These control parameters promote the self-sustained oscillations of the shear layer over inner-flow spanwise waves. As a result, R_{AM} shows

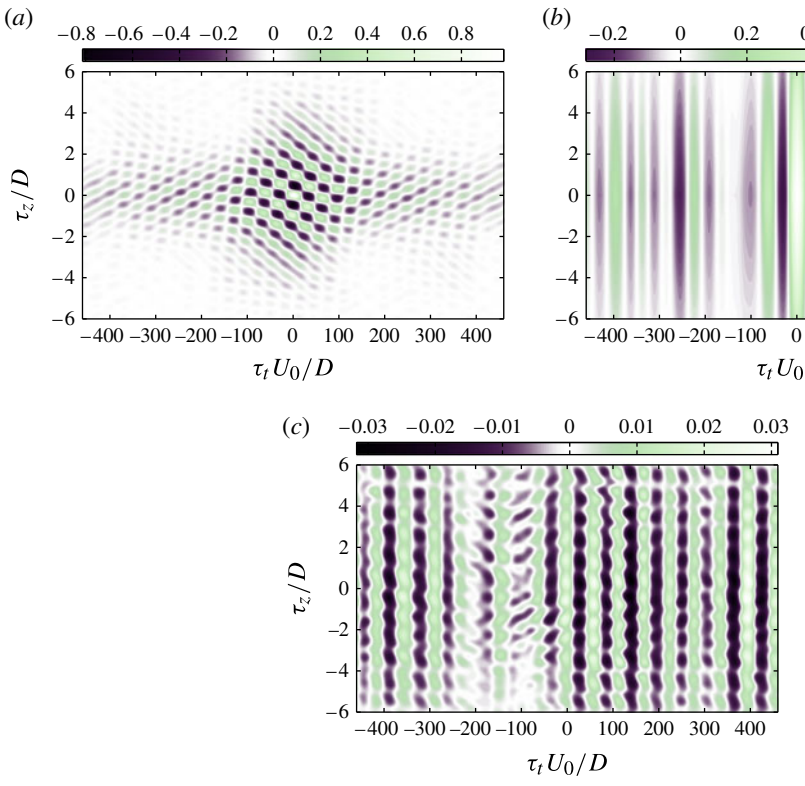

FIGURE 21. (Colour online) Two-dimensional correlations of spanwise–time reconstructed dynamics, extracted at $(x, y) = (1.84\,D, -0.1\,D)$ for the case $L/\theta_0 = 59$, $L/D = 2$, $Re_D = 2400$: (*a*) auto-correlation $R_{CI} \star R_{CI}$; (*b*) auto-correlation $R_{AM} \star R_{AM}$; (*c*) cross-correlation $R_{CI} \star R_{AM}$. Distributions are normalised and $\{\tau_t, \tau_z\}$ are the time and spanwise delays, respectively.

a quasi-periodic temporal signature while the centrifugal instabilities depicted by R_{CI} appear to be strongly distorted. In spite of this change in the prevalence of the two coexisting phenomena, the time cross-correlation $R_{CI} \star R_{AM}$ remains high and basically periodic for all the investigated control parameters, as shown in figure 20(*a–d*) (bottom). The AMs of the shear layer waves remain strongly time correlated with the slow dynamics of the inner flow.

5.2.3. *Spanwise versus temporal modulation*

Considering the three-dimensional structure of the modulating dynamics, the question arises as to how the AM organises along the span of the cavity. The envelope of the shear layer either exhibits spanwise modulations bound to inner-flow centrifugal instabilities, or remains mainly two-dimensional like its carrier waves. To address this question we consider the spanwise correlations of the flow.

Two-dimensional (z, t)-correlations are computed for both $R_{CI}(t, z)$ and $R_{AM}(t, z)$ reconstructed dynamics in figure 21. The auto-correlation of $R_{CI}(t, z)$ in figure 21(*a*) depicts a chessboard-like structure formed by crossing stripes of alternate correlation. This distribution represents the interference patterns produced by the superimposition of the two dominant counter-travelling spanwise waves. The positive slope corresponds

to the right-travelling wave and the negative slope to the left-travelling wave. This salient characteristic of the cavity inner flow has already been reported in Douay *et al.* (2011), Basley (2012) and de Vicente *et al.* (2014). Such an interference is commonly encountered when dealing with centrifugal instabilities. It is worth remarking that the space–time signature of the reconstructed dynamics $R_{CI}(t, z)$ constitutes a (quasi) standing wave. It can therefore be modelled as the idealised form

$$R_{CI}(t, z) \sim A_{sw} \sin(2\pi St_{sw} t') \cos(\beta_{sw} z'), \quad \text{with } t' = t\, U_0/D, \;\; z' = z/D. \tag{5.2}$$

The frequency St_{sw} and the wavenumber β_{sw} depend on the underlying counter-travelling waves. In the present case, one obtains $St_{sw} = 2\pi(St_{\leftarrow} + St_{\rightarrow})/2 \simeq 0.015$ and $\beta_{sw} = (\beta_{\leftarrow} - \beta_{\rightarrow})/2 \simeq 2\pi$. This depicts spanwise oscillations of wavelength D with a beating of the average Strouhal number $St_{sw} = 0.015$, consistent with figures 19(*b*) and 21(*a*).

On the other hand, the auto-correlation of the envelope $R_{AM}(t, z)$ remains two-dimensional with no discernible spanwise scales observed in figure 21(*b*). This indicates that the self-sustained oscillations are alternately enhanced and damped simultaneously everywhere along the span, translating into a strictly temporal AM. This separation between the spanwise waves of the inner flow and the envelope of the shear layer is confirmed by the particularly low (z, t) cross-correlations $R_{CI} \star R_{AM}$, shown in figure 21(*c*). Inner-flow centrifugal instabilities do not influence local vortex shedding. The coupling mechanism responsible for the AMs rather appears to be global. The beating implied by the standing wave of R_{CI} dynamics could be related to this coupling mechanism since it represents a temporal cycle, which is globally undergone by the inner flow. Such a swell might temper the impingement of the vortices shed along the shear layer. Self-sustained oscillations would hence be alternately damped and enhanced as the shear layer respectively avoids or impinges on the trailing edge of the cavity.

6. Concluding remarks

This study brings to light the occurrence of severe AMs of the shear layer waves developing in open cavity flows. The focus is on the lowest modulating frequencies, broad band and typically down to two orders of magnitude below the locked-on frequencies of the shear layer. Amplitude modulations by such very low frequencies are observed consistently and for a wide range of control parameters. The analysis demonstrates that they result from the influence of centrifugal instabilities along the recirculating inner flow. Indeed, this work constitutes one of the few extensive studies dealing with the coexistence of shear layer self-sustained oscillations and centrifugal instabilities in open cavity flows.

The onset of centrifugal instabilities along the recirculating flow leads to slow-moving 3D dynamics, whose most salient features are pairs of counter-propagating spanwise waves. The overlap of these spanwise waves induces interference patterns. In terms of coherent structures, the inner-flow dynamics consists of alleys of spiral vortices pulsating and coiling up around the main recirculation.

The analysis reveals that the inner-flow temporal dynamics and shear layer AMs are highly correlated. Indeed, the bicoherence spectra show that the very-low-frequency 3D waves resulting from centrifugal instabilities exchange significant energy with the locked-on waves of the shear layer through quadratic nonlinearities. It is particularly remarkable that such coherent spanwise fluctuations endure and continue to influence

the high-frequency dynamics of the shear layer despite the increasing strength of the vortex shedding.

The severe temporal modulations of the self-sustained oscillations do not correspond to spanwise modulations: the envelope, modulated in time, remains fairly two-dimensional. It appears that the 3D waves of the inner flow interfere with each other to induce a global modulation of the flow. The notion of a swell is here proposed to refer to a cycle of alternate enhancing/damping of the self-sustained oscillations. Further investigations are necessary to shed more light on the global nature of this coupling mechanism.

Acknowledgements

This work has been supported by Direction Generale de l'Armement and Agence Nationale de la Recherche (project ANR-06-BLAN-0363). The authors would also like to acknowledge the support of this research by the Australian Research Council.

REFERENCES

AIDUN, C. K., TRIANTAFILLOPOULOS, N. G. & BENSON, J. D. 1991 Global stability of a lid-driven cavity with throughflow: flow visualization studies. *Phys. Fluids* A **3**, 2081–2091.

ALBENSOEDER, S. & KUHLMANN, H. C. 2006 Nonlinear three-dimensional flow in the lid-driven square cavity. *J. Fluid Mech.* **569**, 465–480.

ALBENSOEDER, S., KUHLMANN, H. C. & RATH, H. J. 2001 Three-dimensional centrifugal-flow instabilities in the lid-driven-cavity problem. *Phys. Fluids* **13**, 121–135.

BARKLEY, D., GOMES, M. G. M. & HENDERSON, R. D. 2002 Three-dimensional instability in flow over a backward-facing step. *J. Fluid Mech.* **473**, 167–190.

BASLEY, J. 2012 An experimental investigation on waves and coherent structures in a three-dimensional open cavity flow. PhD thesis, Université Paris-Sud (Orsay, France) & Monash University (Melbourne, Australia).

BASLEY, J., PASTUR, L. R., DELPRAT, N. & LUSSEYRAN, F. 2013 Space–time aspects of a three-dimensional multi-modulated open cavity flow. *Phys. Fluids* **25** (6), 064105.

BASLEY, J., PASTUR, L. R., LUSSEYRAN, F., FAURE, T. M. & DELPRAT, N. 2011 Experimental investigation of global structures in an incompressible cavity flow using time-resolved PIV. *Exp. Fluids* **50**, 905–918.

BASLEY, J., SORIA, J., PASTUR, L. R. & LUSSEYRAN, F. 2014 Three-dimensional waves inside an open cavity and interactions with the impinging shear layer. In *Fluid Mechanics and its Applications*, vol. 107. Springer.

BEAUDOIN, J.-F., CADOT, O., AIDER, J.-L. & WESFREID, J. E. 2004 Three-dimensional stationary flow over a backward-facing step. *Eur. J. Mech. (*B*/Fluids)* **23**, 147–155.

BENNEY, D. J. & LIN, C. C. 1960 On the secondary motion induced by oscillations in a shear flow. *Phys. Fluids* **3**, 656–657.

BLACKBURN, H. M. & LOPEZ, J. M. 2003 The onset of three-dimensional standing and modulated travelling waves in a periodically driven cavity flow. *J. Fluid Mech.* **497**, 289–317.

BÖDEWADT, U. T. 1940 *Z. Angew. Math. Mech.* **20**, 241–253.

BRÈS, G. A. & COLONIUS, T. 2008 Three-dimensional instabilities in compressible flow over open cavities. *J. Fluid Mech.* **599**, 309–339.

BUCHMANN, N. A., ATKINSON, C. & SORIA, S. 2013 Influence of ZNMF jet flow control on the spatio-temporal flow structure over a NACA-0015 airfoil. *Exp. Fluids* **54** (3), 1–14.

CAMMILLERI, A., GUENIAT, F., CARLIER, J., PASTUR, L., MEMIN, E., LUSSEYRAN, F. & ARTANA, G. 2013 Pod-spectral decomposition for fluid flow analysis and model reduction. *Theor. Comput. Fluid Dyn.* **27**, 787–815.

CHANG, K., CONSTANTINESCU, G. & PARK, S.-O. 2006 Analysis of the flow and mass transfer processes for the incompressible flow past an open cavity with a laminar and a fully turbulent incoming boundary layer. *J. Fluid Mech.* **561**, 113–145.

CHIANG, T., SHEU, W. & HWANG, R. 1998 Effects of the Reynolds number on the eddy structure in a lid-driven cavity. *Intl J. Numer. Meth. Fluids* **26**, 557–579.

CORDIER, L. & BERGMANN, M. 2003 Proper orthogonal decomposition: an overview. In *VKI Lecture Series (2003-03): Post Processing of Experimental and Numerical Data*.

DELPRAT, N. 2006 Rossiter formula: a simple spectral model for a complex amplitude modulation process? *Phys. Fluids* **18**, 071703.

DELPRAT, N. 2010 Low-frequency components and modulation processes in compressible cavity flows. *J. Sound Vib.* **329** (22), 4797–4809.

DOUAY, C. L., GUÉNIAT, F., PASTUR, L., LUSSEYRAN, F. & FAURE, T. M. 2011 Instabilités centrifuges dans un écoulement de cavité: décomposition en modes dynamiques. In *Comptes-Rendus des Rencontres du Non-linéaire*, vol. 14, pp. 47–52.

FAURE, T. M., ADRIANOS, P., LUSSEYRAN, F. & PASTUR, L. R. 2007 Visualizations of the flow inside an open cavity at medium range Reynolds numbers. *Exp. Fluids* **42** (2), 169–184.

FAURE, T. M., PASTUR, L. R., LUSSEYRAN, F., FRAIGNEAU, Y. & BISCH, D. 2009 Three-dimensional centrifugal instabilities development inside a parallelepipedic open cavity of various shape. *Exp. Fluids* **47** (3), 395–410.

FERNANDEZ-FERIA, R. 2000 Axisymmetric instabilities of Bödewadt flow. *Phys. Fluids* **12**, 1730.

GLOERFELT, X. 2006 Compressible pod/Galerkin reduced-order model of self-sustained oscillations in a cavity. *AIAA Paper* 2006 (2433).

GLOERFELT, X. 2008 Compressible proper orthogonal decomposition/Galerkin reduced-order model of self-sustained oscillations in a cavity. *Phys. Fluids* **20** (11), 115105.

GONZALEZ, L. M., AHMED, M., KÜHNEN, J., KUHLMANN, H. C. & THEOFILIS, V. 2011 Three-dimensional flow instability in a lid-driven isosceles triangular cavity. *J. Fluid Mech.* **675**, 369–396.

GÖRTLER, H. 1955 *Fifty Years of Boundary Layer Research*. Vieweg and Son.

GUÉNIAT, F., PASTUR, L. & LUSSEYRAN, F. 2014 Investigating mode competition and three-dimensional features from two-dimensional velocity fields in an open cavity flow by modal decompositions. *Phys. Fluids* **26** (8), 085101.

GUERMOND, J.-L., MIGEON, C., PINEAU, G. & QUARTAPELLE, L. 2002 Start-up flows in a three-dimensional rectangular driven cavity of aspect ratio 1:1:2 at $Re = 1000$. *J. Fluid Mech.* **450**, 169–199.

HOLMES, P., LUMLEY, J. L. & BERKOOZ, G. 1996 *Turbulence, Coherent Structures, Dynamical Systems and Symmetry*. Cambridge University press.

HUANG, N. E., LONG, S. R. & SHEN, Z. 1996 The mechanism for frequency downshift in nonlinear wave evolution. *Adv. Appl. Mech.* **32**, 59–111.

HUANG, N. E., SHEN, Z. & LONG, S. R. 1999 A new view of nonlinear water waves: the Hilbert spectrum. *Annu. Rev. Fluid Mech.* **31**, 417–457.

HUANG, N. E., SHEN, Z., LONG, S. R., WU, M. C., SHIH, H. H., ZHENG, Q., YEN, N.-C., TUNG, C. C. & LIU, H. H. 1998 The empirical mode decomposition and Hilbert spectrum for nonlinear and non-stationary time-series analysis. *Proc. R. Soc. Lond.* A **454**, 903–995.

ISAACSON, L. K. & MARSHALL, A. G. 1983 Nonlinear resonant interactions in internal cavity flows. *AIAA J.* **21** (5), 785–786.

IUNGO, G. V. & LOMBARDI, E. 2011 A procedure based on proper orthogonal decomposition for time–frequency analysis of time series. *Exp. Fluids* **51**, 969–985.

JIMENEZ, J. 1983 A spanwise structure in a plane shear layer. *J. Fluid Mech.* **132**, 319–336.

KEGERISE, M. A., SPINA, E. F., GARG, S. & CATTAFESTA III, L. N. 2004 Mode-switching and nonlinear effects in compressible flow over a cavity. *Phys. Fluids* **16**, 678–687.

KIM, Y. C., BEALL, J. M., POWERS, E. J. & MIKSAD, R. W. 1980 Bispectrum and nonlinear wave coupling. *Phys. Fluids* **23** (2), 258–263.

KITSIOS, V., CORDIER, L., BONNET, J.-P., OOI, A. & SORIA, J. 2011 On the coherent structures and stability properties of a leading-edge separated aerofoil with turbulent recirculation. *J. Fluid Mech.* **683**, 395–416.

KNISELY, C. & ROCKWELL, D. 1982 Self-sustained low-frequency components in an impinging shear layer. *J. Fluid Mech.* **116**, 157–186.

KOSEFF, J. R. & STREET, R. L. 1984*a* The lid-driven cavity flow: a synthesis of qualitative and quantitative observations. *Trans. ASME J. Fluids Engng* **106**, 390–398.

KOSEFF, J. R. & STREET, R. L. 1984*b* On endwall effects in a lid-driven cavity flow. *Trans. ASME: J. Fluids Engng* **106**, 385–389.

KOSEFF, J. R. & STREET, R. L. 1984*c* Visualization studies of a shear driven three-dimensional recirculating flow. *Trans. ASME: J. Fluids Engng* **106**, 21–29.

KUHLMANN, H. C., WANSCHURA, M. & RATH, H. J. 1997 Flow in two-sided lid-driven cavities: non-uniqueness, instabilities, and cellular structures. *J. Fluid Mech.* **336**, 267–299.

LARCHEVÊQUE, L., SAGAUT, P. & LABBÉ, O. 2007 Large-eddy simulation of a subsonic cavity flow including asymmetric three-dimensional effects. *J. Fluid Mech.* **577**, 105–126.

LARCHEVÊQUE, L., SAGAUT, P., LÊ, T. H. & COMTE, P. 2004 Large-eddy simulations of a compressible flow in a 3D open cavity at high Reynolds number. *J. Fluid Mech.* **516**, 265–301.

LASHERAS, J. C. & CHOI, H. 1988 Three-dimensional instability of a plane free shear layer: an experimental study of the formation and evolution of streamwise vortices. *J. Fluid Mech.* **189**, 53–86.

LUSSEYRAN, F., PASTUR, L. & LETELLIER, C. 2008 Dynamical analysis of an intermittency in an open cavity flow. *Phys. Fluids* **20** (11), 114101.

MALONE, J., DEBIASI, M., LITTLE, J. & SAMIMY, M. 2009 Analysis of the spectral relationships of cavity tones in subsonic resonant cavity flows. *Phys. Fluids* **21** (5), 055103.

MESEGUER-GARRIDO, F., DE VICENTE, J., VALERO, E. & THEOFILIS, V. 2011 Effect of aspect ratio on the three-dimensional global instability analysis of incompressible open cavity flows. *AIAA Paper* 2011 (3605).

MESEGUER-GARRIDO, F., DE VICENTE, J., VALERO, E. & THEOFILIS, V. 2014 On linear instability mechanisms in incompressible open cavity flow. *J. Fluid Mech.* **752**, 219–236.

METCALFE, R. W., ORSZAG, S. A., BRACHET, M. E., MENON, S. & RILEY, J. J. 1987 Secondary instability of a temporally growing mixing layer. *J. Fluid Mech.* **184**, 207–243.

MIGEON, C., PINEAU, G. & TEXIER, A. 2003 Three-dimensionality development inside standard parallelepipedic lid-driven cavities at $Re = 1000$. *J. Fluids Struct.* **17**, 717–738.

MIKSAD, R. W. 1972 Experiments on nonlinear stages of free shear layer transition. *J. Fluid Mech.* **56** (4), 695–719.

NEARY, M. D. & STEPHANOFF, K. D. 1987 Shear-layer-driven transition in a rectangular cavity. *Phys. Fluids* **30** (10), 2936–2946.

PASTUR, L. R., LUSSEYRAN, F., FAURE, T. M., FRAIGNEAU, Y., PETHIEU, R. & DEBESSE, P. 2008 Quantifying the nonlinear mode competition in the flow over an open cavity at medium Reynolds number. *Exp. Fluids* **44** (4), 597–608.

PASTUR, L. R., LUSSEYRAN, F., FRAIGNEAU, Y. & PODVIN, B. 2005 Determining the spectral signature of spatial coherent structures in an open cavity flow. *Phys. Rev.* E **72**, 065301(R).

PEREIRA, J. C. F. & SOUSA, J. J. M. 1995 Experimental and numerical investigation of flow oscillations in a rectangular cavity. *Trans. ASME: J. Fluids Engng* **117** (1), 68–74.

PODVIN, B., FRAIGNEAU, Y., LUSSEYRAN, F. & GOUGAT, P. 2006 A reconstruction method for the flow past an open cavity. *Trans. ASME: J. Fluids Engng* **128**, 531–540.

POWELL, A. 1953 On edge tones and associated phenomena. *Acustica* **3**, 233–243.

POWELL, A. 1961 On the edgetone. *J. Acoust. Soc. Am.* **33**, 395–409.

POWELL, A. 1995 Lord Rayleigh's foundations of aeroacoustics. *J. Acoust. Soc. Am.* **98**, 1839–1844.

RAMANAN, N. & HOMSY, G. M. 1994 Linear stability of lid-driven cavity flow. *Phys. Fluids* **6**, 2690–2701.

ROCKWELL, D. 1977 Prediction of oscillation frequencies for unstable flow past cavities. *Trans. ASME: J. Fluids Engng* **99**, 294–300.

ROCKWELL, D. & KNISELY, C. 1980 Observations of the three-dimensional nature of unstable flow past a cavity. *Phys. Fluids* **23**, 425–431.

ROCKWELL, D. & NAUDASCHER, E. 1978 Review – self-sustaining oscillations of flow past cavities. *Trans. ASME: J. Fluids Engng* **100**, 152–165.

ROCKWELL, D. & NAUDASCHER, E. 1979 Self-sustained oscillations of impinging free shear layers. *Annu. Rev. Fluid Mech.* **11**, 67–94.

ROSSITER, J. 1964 Wind-tunnel experiments on the flow over rectangular cavities at subsonic and transonic speeds. *Aeronautical Research Council Report No.* 3438.

ROWLEY, C. W., COLONIUS, T. & BASU, A. J. 2002 On self-sustained oscillations in two-dimensional compressible flow over rectangular cavities. *J. Fluid Mech.* **455**, 315–346.

ROWLEY, C. W., COLONIUS, T. & MURRAY, R. M. 2000 Pod based model of self-sustained oscillations in the flow past an open cavity. *AIAA Paper* 2000; (1969).

SAROHIA, V. 1977 Experimental investigation of oscillations in flows over shallow cavities. *AIAA J.* **15** (7), 984–991.

SIPP, D. & JACQUIN, L. 2000 Three-dimensional centrifugal-type instabilities of two-dimensional flows in rotating systems. *Phys. Fluids* **12**, 1740–1748.

SORIA, J. 1996 An investigation of the near wake of a circular cylinder using a video-based digital cross-correlation particle image velocimetry technique. *Exp. Therm. Fluid Sci.* **12**, 221–233.

SORIA, J. 1998 Multigrid approach to cross-correlation digital PIV and HPIV analysis. In *Australasian Fluid Mechanics Conference*, vol. 13. Monash University.

SORIA, J., CATER, J. & KOSTAS, J. 1999 High resolution multigrid cross-correlation digital PIV measurements of a turbulent starting jet using half frame image shift film recording. *Opt Laser Technol.* **31**, 3–12.

TAYLOR, G. I. 1923 Three-dimensional flow instability in a lid-driven isosceles triangular cavity. *Phil. Trans.* A **223**, 289.

THEOFILIS, V. 2003 Advances in global linear instability of non-parallel and three-dimensional flows. *Prog. Aerosp. Sci.* **39** (4), 249–315.

THEOFILIS, V., DUCK, P. W. & OWEN, J. 2004 Viscous linear stability analysis of rectangular duct and cavity flows. *J. Fluid Mech.* **505**, 249–286.

DE VICENTE, J. 2010 Spectral multi-domain method for the global instability analysis of complex cavity flows. PhD thesis, Universidad Politécnica de Madrid.

DE VICENTE, J., BASLEY, J., MESEGUER-GARRIDO, F., SORIA, J. & THEOFILIS, V. 2014 Three-dimensional instabilities over a rectangular open cavity: from linear stability analysis to experimentation. *J. Fluid Mech.* **748**, 189–220.

VIKRAMADITYA, N. S. & KURIAN, J. 2012 Nonlinear aspects of supersonic flow past a cavity. *Exp. Fluids* **52**, 1389–1399.

VOGEL, M., HIRSA, A. H. & LOPEZ, J. M. 2003 Spatio-temporal dynamics of a periodically driven cavity flow. *J. Fluid Mech.* **478**, 197–226.

WELCH, P. D. 1967 The use of fast Fourier treansform for the estimation of power spectra: a method based on time averaging over short, modified periodograms. In *Modern spectrum analysis*, pp. 17–20. IEEE Press.

WOO, C.-H., KIM, J.-S. & LEE, K.-H. 2007 Three-dimensional effects of supersonic cavity flow due to the variation of cavity aspect and width ratios. *J. Mech. Sci. Technol.* **22**, 590–598.

YAMOUNI, S., SIPP, D. & JACQUIN, L. 2013 Interaction between feedback aeroacoustic and acoustic resonance mechanisms in a cavity flow: a global stability analysis. *J. Fluid Mech.* **717**, 134–165.

ZIADA, S. & ROCKWELL, D. 1982 Oscillations of an unstable mixing layer impinging upon an edge. *J. Fluid Mech.* **124**, 307–334.